AIAA JOURNAL
Vol. 47, No. 1, January 2009

Large-Eddy Simulation of Self-Sustained Flow Instabilities in Cavities Using the Lattice-Boltzmann Method

Kannan N. Premnath* and Martin J. Pattison†
MetaHeuristics LLC, Santa Barbara, California 93105
and
Sanjoy Banerjee‡
University of California, Santa Barbara, Santa Barbara, California 93106

DOI: 10.2514/1.38278

Three-dimensional large-eddy simulations of flows past cavities are performed by solving a generalized lattice-Boltzmann equation, which is based on multiple relaxation times. To incorporate subgrid-scale turbulence effects in this equation, its hydrodynamic relaxation time scales are modified by the eddy viscosity Smagorinsky model, which is modulated near walls by the van Driest damping function. The relaxation times for kinetic modes are adjusted to enhance its numerical stability at higher Reynolds numbers. Parallel computations of subsonic compressible flow over cavities of different configurations (shallow and deep, with and without a splitter plate) are performed to investigate self-sustained resonant flow instabilities and generation of tones. Computed flow patterns and flow oscillation frequencies in the shear-layer region for these problems are found to be in good agreement with previous computational simulations and experiments. When possible, detailed comparisons of the components of the root-mean-square velocity fluctuations have also been made, and reasonably good agreement with data from a previous computational study has been found. The computational approach exhibited near-linear parallel scalability on a parallel cluster.

I. Introduction

FLOWS past cavities are known to lead to self-sustained oscillations and noise generation under a range of physical conditions and geometric configurations. Such complex fluid-dynamic phenomena have been a subject of great interest due to their occurrence in a variety of applications. In particular, flow instabilities and noise generation in cavities are canonical representations of flow-induced noise in components of aviation systems such as weapon bays, wheel wells in landing gear, and instrumentation compartments, in which they can potentially cause structural damage and optical distortion problems. They are also common in automotive systems such as sunroofs, open windows and door seals, and in underwater-vehicle systems. Noise reduction in such applications is not only of strategic importance, but is often required to ensure safer and environmentally conscious transportation systems such as those as envisioned by NASA and the aviation industry. In this regard, analytical techniques, experimental investigations, and computational methods play an important role in the fundamental understanding of the underlying complex character of the interaction of fluid dynamics and acoustics. Moreover, various passive and active flow control techniques have been employed for noise suppression in cavity cutouts.

Some of the pioneering experimental studies on cavity flows were carried out over 50 years ago by Krishnamurty [1] and Roskho [2]. Measurements of flows and associated instabilities were performed under a broader range of conditions and configurations by Maull and East [3] and Rossiter [4] and continued by several researchers over the years [5–11]. Cavity flows are often characterized by shear-layer instabilities in the mouth of the cavity that excite acoustic modes, which reinforce the flow oscillations (i.e., resulting in a feedback process). The essential mechanism of tone generation from cavities in terms of such a simple feedback process was first discussed by Rossiter [4], who also provided a semi-empirical expression to calculate the tonal resonant frequencies. It may be noted that under certain specialized conditions, a different type of instability termed the wake mode, which can result in increased drag on the cavity due to impingement and ejections of large vortical structures, was observed by Gharib and Roskho [12]. Analytical models to characterize the frequencies of the modes of oscillations in cavities were developed by, for example, Bilanin and Covert [13], Tam and Block [14], and Howe [15].

An illuminating and comprehensive review of the earlier investigations was provided by Rockwell and Naudascher [16], who classified various types of possible flow instabilities and acoustic phenomena in cavities. According to them, in broad terms, flow oscillations occurring in a cavity can be characterized as fluid-dynamic, fluid-resonant, or fluid-elastic. Fluid-dynamic oscillations originate from the instabilities associated with mixing or shear layers in the opening of the cavity that are amplified and sustained through acoustic pressure propagation. On the other hand, fluid-resonant oscillations occur due to resonant waves established by the cavity geometry. Fluid-elastic oscillations can be generated due to fluctuations of the cavity surfaces. Depending on the cavity geometry (such as its aspect ratio) and the flow conditions (such as the Reynolds number, Mach number, and the momentum thickness of the upstream boundary layer), one or more of these types of oscillations and instabilities can lead to a discrete tone or set of tones.

Computational studies of cavity flows are crucial to the detailed understanding of flow instabilities in cavities. Earlier computational efforts were generally two-dimensional (2-D) and often employed Reynolds-averaged Navier–Stokes (RANS) models to represent turbulence effects [17–20]. It is unclear if such coarse-grained models are robust in the context of strongly time-dependent oscillating flows involving separation and sound radiation, which are

Received 26 April 2008; revision received 23 September 2008; accepted for publication 9 October 2008.

*Senior Engineer, 3944 State Street, Suite 350; Research Associate, University of California, Santa Barbara, Santa Barbara, CA 93106.
†Senior Engineer, 3944 State Street, Suite 350.
‡Professor, Department of Chemical Engineering; Department of Mechanical Engineering, Bren School of Environmental Science and Management.

characteristic of cavity flows. On the other hand, direct numerical simulations (DNS) resolve all spatial and temporal scales and can thus predict all possible fluid motions up to dissipation length scales with high fidelity. However, the computational cost of DNS limits its utility to relatively low Reynolds numbers. Indeed, in a series of seminal papers, Colonius et al. [21,22] and Rowley et al. [23] performed DNS in two dimensions and, more recently, in three dimensions (3-D) [24], which provided fundamental insights into fluid motions and instabilities in cavities at relatively low Reynolds numbers.

It is often more practical to use large-eddy simulation (LES), in which fluid motions with length scales greater than the grid size are computed and the effect of the unresolved eddies at subgrid scales (SGS) are modeled. As such, large scales represent the anisotropic part of the energy spectrum and contain most of the energy of the fluid motions. The smaller SGS scales are generally considered to be isotropic in nature and relatively independent of the resolved part of the spectrum. Thus, LES represents a compromise with reduced empiricism in contrast to RANS models and with reduced computational cost in comparison with DNS.

More recently, there has been much interest in the 3-D LES using filtered Navier–Stokes equations with a SGS model, such as the Smagorinsky eddy viscosity model [25] for cavity flows. Examples include those by Dubief and Delcayre [26], Gloerfelt et al. [27], Larcheveque et al. [28,29], and Suponitsky et al. [30]. It may be noted that a variant of this theme is to use a hybrid approach in which the turbulence model in the near-wall region behaves as a RANS model, but switches its role to a SGS model in the outer or bulk flow region. This is often termed as the detached eddy simulation (DES) approach. Shieh and Morris [31] performed DES of cavity flows using the Spalart–Allmaras model [32].

Generally, wake-mode instability was observed mainly in 2-D computations, and shear-layer or Rossiter instability was found to be the dominant mechanism, particularly in 3-D simulations. Colonius [33] and Rowley and Williams [34] reviewed various computational studies and flow control strategies for flow and acoustic instabilities in cavity flows.

In the present work, we employ an alternative computational method based on the lattice-Boltzmann method (LBM) to perform LES of 3-D fluid motions and associated instabilities from flow past cavities in a variety of configurations. The LBM, which is based on kinetic theory, is a relatively recent approach for computational fluid dynamics and other problems [35,36]. It involves solving a kinetic equation, the lattice-Boltzmann equation (LBE), which represents the propagation of particle populations along discrete directions and collisions on a lattice. The long-term spatial and temporal dynamics of the LBE asymptotically corresponds to the fluid flow described by the weakly compressible Navier–Stokes equations when the lattice is constructed to respect sufficient rotational symmetries. The attractiveness of LBM comes from the simplicity of the stream-and-collide computational procedure, its ability to represent boundary conditions in complex geometries, the natural amenability for implementation on parallel computers with near-linear scalability, and its ability to more naturally model complex physics derived from kinetic theory. As a result, it has found a wide variety of applications (see, for example, [37–39]). More recently, there have been several efforts that have substantially improved the basic features of the LBM, notably, in the areas of turbulence modeling [40,41], higher-order and thermal effects [42,43], and involving novel entropic approaches [44]. Moreover, the LBM has been demonstrated to be a reliable method for computation of sound wave propagation [45,46] and has more recently been successfully employed for computation of various aeroacoustics problems [47–53].

A commonly used form of the LBM employs a single-relaxation-time (SRT) model [54] to represent the effect of particle collisions, in which particle distributions relax to their local equilibrium at a rate determined by a single parameter [55,56]. On the other hand, an equivalent representation of distribution functions is in terms of their moments such as various hydrodynamic fields, including density, mass flux, and stress tensor. The relaxation process due to collisions can more naturally be described in terms of a space spanned by such moments, which can, in general, relax at different rates. This forms the basis of the generalized lattice-Boltzmann equation (GLBE), which employs a multiple-relaxation-time (MRT) model to represent the collision process [57–59]. By carefully separating the time scales of various hydrodynamic and kinetic modes through a linear stability analysis, the numerical stability of the GLBE or MRT–LBE can be significantly improved when compared with the SRT–LBE, particularly for more demanding problems at high Reynolds numbers [58]. The MRT–LBE has also been extended for multiphase flows with superior stability characteristics [60–62], and, more recently, for magnetohydrodynamic problems with similar results [63]. It has also been used for LES of a class of turbulent flows [64,65].

Recently, we have extended the GLBE to incorporate forcing terms and applied it to wall-bounded turbulent flows [66]. These forcing terms represent the effect of external forces and are considered in the natural moment space of the GLBE. They are second-order time-discretized to avoid discrete lattice artifacts [67] and made effectively explicit through a transformation [68] to facilitate numerical solution. Subgrid-scale effects are represented by the standard Smagorinsky eddy viscosity model [25], which is modified by the van Driest damping function [69] in the near-wall region. The strain-rate tensor used on the SGS model is computed in terms of nonequilibrium moments, which is augmented by the moment representation of forcing terms in this approach.

It is well known that for wall-bounded flows, standard LES requires resolution of near-wall energy containing eddies as in DNS, with at least 3 grid nodes in the viscous sublayer [70,71]. This can impose severe computational requirements, particularly at high Reynolds numbers Re [i.e., $\mathcal{O}(10^5)$–(10^6)]. One way to circumvent this situation is to employ a wall model in which the first off-wall grid node is located well into the logarithmic region, as was done by Larcheveque et al. [28,29] for cavity flows. However, in the present work, we will consider wall-resolved 3-D LES of cavity flows at moderate Reynolds numbers [i.e., $\mathcal{O}(10^4)$]. Although a few previous studies exist for such moderate Reynolds numbers using other computational methods, such as that by Gloerfelt et al. [27] and Suponitsky et al. [30], the focus will be on the application of a recent variant of the LBM (i.e., the GLBE [59,61,66]) for LES of cavity flows of different configurations. Toward this objective, we will study the physics of flow past both shallow and deep cavities at Reynolds numbers (based on cavity width) of 17,500 and 10,450, respectively, and perform detailed comparisons of the frequencies as well as the intensities of flow oscillations when previous data are available. To simulate relatively large problems involving cavity flows, we have exploited the inherent parallelization properties of the GLBE and implemented it on a parallel cluster to investigate associated self-sustained flow instabilities and oscillations in detail and provide comparison with previous data.

The paper is organized as follows: Section II will discuss the overall computational procedure based on the GLBE. The SGS turbulence model employed for LES using the GLBE is presented in Sec. III. The boundary conditions used in this study are provided in Sec. IV. Section V discusses parallel implementation of the computational approach. Results of cavity flow characteristics, including tonal frequencies, under various configurations will be presented in Sec. VI. In particular, Sec. VI.A discusses flow instabilities in a deep cavity with a splitter plate, Sec. VI.B presents results of flows and oscillations in a shallow cavity, and Sec. VI.C presents simulation of flow past a deep cavity without splitter plate. Finally, the conclusions of this paper are presented in Sec. VII.

II. Generalized Lattice-Boltzmann Equation

The lattice-Boltzmann method computes the evolution of distribution functions due to the collision process given in terms of a relaxation to their local equilibrium and the streaming process describing their movement along the characteristic directions given by a discrete particle velocity space represented by a lattice. Figure 1 shows the three-dimensional 19-particle velocity (D3Q19) lattice

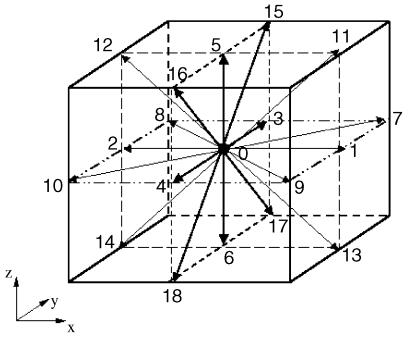

Fig. 1 Schematic illustration of the three-dimensional 19-particle velocity (D3Q19) lattice model.

model, which has better stability characteristics than other lattice models such as the D3Q15 model, has been employed in this paper. The particle velocity set $\mathbf{e}_\alpha$ corresponding to this model may be written as

$$\mathbf{e}_\alpha = \begin{cases} (0,0,0) & \alpha = 0 \\ (\pm 1,0,0),\ (0,\pm 1,0),\ (0,0,\pm 1) & \alpha = 1,\ldots,6 \\ (\pm 1,\pm 1,0),\ (\pm 1,0,\pm 1),\ (0,\pm 1,\pm 1) & \alpha = 7,\ldots,18 \end{cases} \tag{1}$$

The GLBE computes collisions in moment space, whereas the streaming process is done in the usual particle velocity space [59]. The GLBE also computes the forcing term [66], which represents the effect of external body forces as a second-order-accurate time discretization in moment space. Such external forces acting on the fluid could be gravity or inertial forces such as the Coriolis force. We use the following notation in our description of the subsequent procedure: in *particle velocity space*, the local distribution function $\mathbf{f}$, its local equilibrium distribution $\mathbf{f}^{\mathrm{eq}}$, and the source terms due to external forces $\mathbf{S}$ may be written as the following column vectors:

$$\mathbf{f} = [f_0, f_1, f_2, \ldots, f_{18}]^\dagger, \qquad \mathbf{f}^{\mathrm{eq}} = \left[f_0^{\mathrm{eq}}, f_1^{\mathrm{eq}}, f_2^{\mathrm{eq}}, \ldots, f_{18}^{\mathrm{eq}}\right]^\dagger$$
$$\mathbf{S} = [S_0, S_1, S_2, \ldots, S_{18}]^\dagger$$

where superscript † represents the transpose operator.

The moments $\hat{\mathbf{f}}$ are related to the distribution function $\mathbf{f}$ through the relation $\hat{\mathbf{f}} = \mathcal{T}\mathbf{f}$, where $\mathcal{T}$ is the transformation matrix. Here and in the following, the hat represents the moment space. The transformation matrix $\mathcal{T}$ is constructed such that the collision matrix in moment space $\hat{\Lambda}$ is a diagonal matrix through $\hat{\Lambda} = \mathcal{T}\Lambda\mathcal{T}^{-1}$, where Λ is the collision matrix in particle velocity space. The elements of $\mathcal{T}$ are obtained in a suitable orthogonal basis as combinations of monomials of the Cartesian components of the particle velocity $\mathbf{e}_\alpha$ through the standard Gram–Schmidt procedure, which are provided by d'Humières et al. [59]. Similarly, the equilibrium moments and the source terms in moment space may be obtained through the transformation $\hat{\mathbf{f}}^{\mathrm{eq}} = \mathcal{T}\mathbf{f}^{\mathrm{eq}}$ and $\hat{\mathbf{S}} = \mathcal{T}\mathbf{S}$. The components of the moment projections of these quantities are

$$\hat{\mathbf{f}} = [\hat{f}_0, \hat{f}_1, \hat{f}_2, \ldots, \hat{f}_{18}]^\dagger, \qquad \hat{\mathbf{f}}^{\mathrm{eq}} = \left[\hat{f}_0^{\mathrm{eq}}, \hat{f}_1^{\mathrm{eq}}, \hat{f}_2^{\mathrm{eq}}, \ldots, \hat{f}_{18}^{\mathrm{eq}}\right]^\dagger$$
$$\hat{\mathbf{S}} = [\hat{S}_0, \hat{S}_1, \hat{S}_2, \ldots, \hat{S}_{18}]^\dagger$$

These are provided in the Appendix.

The solution of the GLBE with forcing term can be written in terms of the following effective collision and streaming steps, respectively:

$$\tilde{\mathbf{f}}(\mathbf{x}, t) = \mathbf{f}(\mathbf{x}, t) + \boldsymbol{\varpi}(\mathbf{x}, t) \tag{2}$$

and

$$f_\alpha(\mathbf{x} + \mathbf{e}_\alpha \delta_t, t + \delta_t) = \tilde{f}_\alpha(\mathbf{x}, t) \tag{3}$$

where the distribution function $\mathbf{f} = \{f_\alpha\}_{\alpha=0,1,\ldots,18}$ is updated due to effective collision resulting in the postcollision distribution function $\tilde{\mathbf{f}} = \{\tilde{f}_\alpha\}_{\alpha=0,1,\ldots,18}$ before being shifted along the characteristic directions during the streaming step; $\boldsymbol{\varpi}$ represents the change in distribution function due to collisions as a relaxation process and external forces and, following Premnath et al.[66], it can written as

$$\boldsymbol{\varpi}(\mathbf{x}, t) = \mathcal{T}^{-1}[-\hat{\Lambda}(\hat{\mathbf{f}} - \hat{\mathbf{f}}^{\mathrm{eq}})_{(\mathbf{x},t)} + (\mathcal{I} - \tfrac{1}{2}\hat{\Lambda})\hat{\mathbf{S}}_{(\mathbf{x},t)}] \tag{4}$$

where $\mathcal{I}$ is the identity matrix and $\hat{\Lambda} = \mathrm{diag}(s_0, s_1, \ldots, s_{18})$ is the diagonal collision matrix in moment space. Now some of the relaxation times s_α in the collision matrix (i.e., those corresponding to hydrodynamic modes) can be related to the transport coefficients and modulated by eddy viscosity due to SGS effects (discussed in the next section) as follows [59,66]: $s_1^{-1} = \frac{9}{2}\zeta + \frac{1}{2}$, where ζ is the molecular bulk viscosity, and

$$s_9 = s_{11} = s_{13} = s_{14} = s_{15} = s_\nu$$

where

$$s_\nu^{-1} = 3\nu + \tfrac{1}{2} = 3(\nu_0 + \nu_t) + \tfrac{1}{2}$$

where ν_0 is the molecular shear viscosity and ν_t is the eddy viscosity determined from the SGS model. The rest of the relaxation parameters (i.e., for the kinetic modes) can be chosen through a von Neumann stability analysis of the linearized GLBE [59]:

$$s_1 = 1.19, \qquad s_2 = s_{10} = s_{12} = 1.4, \qquad s_4 = s_6 = s_8 = 1.2$$
$$s_{16} = s_{17} = s_{18} = 1.98$$

.

Once the distribution function is known, the hydrodynamic fields (viz., the density ρ, velocity $\mathbf{u}$, and pressure p) can be obtained as follows:

$$\rho = \sum_{\alpha=0}^{18} f_\alpha, \qquad \mathbf{j} \equiv \rho\mathbf{u} = \sum_{\alpha=0}^{18} f_\alpha \mathbf{e}_\alpha + \frac{1}{2}\mathbf{F}\delta_t, \qquad p = c_s^2\rho \tag{5}$$

where $c_s = c/\sqrt{3}$ ($c = \delta_x/\delta_t$) is the particle speed, and δ_x and δ_t are the lattice spacing and time step, respectively. By means of the Chapman–Enskog multiscale analysis, it can be shown that the GLBE asymptotically recovers the hydrodynamic fields [i.e., Eq. (5)] corresponds to the weakly compressible Navier–Stokes equations.

The computational procedure for the solution of the GLBE with forcing term is optimized by fully exploiting the special properties of the transformation matrix $\mathcal{T}$: these include its orthogonality, the presence of many elements that are zero, and entries with many common integer elements, which are used to form the most common subexpressions for transformation between spaces in avoiding direct matrix multiplications [59]. For details, we refer the reader to [66]. As a result of such optimizations, the additional computational overhead when the GLBE is used in lieu of the popular SRT–LBE is small, typically between 15 and 30%, but with much enhanced numerical stability that allows maintaining solution fidelity on coarser grids and also in simulating flows at higher Reynolds numbers.

III. Subgrid-Scale Turbulence Model

In this paper, we have incorporated the SGS effects in the GLBE through the standard Smagorinsky model [25] to perform LES. The eddy viscosity ν_t arising from this model can be written as

$$\nu_t = (C_s\Delta)^2\bar{S}, \qquad \bar{S} = \sqrt{2S_{ij}S_{ij}} \tag{6}$$

where C_s is a constant (taken equal to 0.12 for the work discussed here), Δ is the cutoff length scale set equal to the lattice-grid spacing (i.e., $\Delta = \delta_x$), and S_{ij} is the strain-rate tensor given by $S_{ij} = 1/2(\partial_j u_i + \partial_i u_j)$. In the LBM, the strain-rate tensor can be computed directly from the nonequilibrium part of the moments,

without the need to apply finite differencing of the velocity field. The specific expressions for the strain-rate tensor as a function of nonequilibrium moments and moment projections of source terms are given in the Appendix. The eddy viscosity ν_t thus obtained is added to the molecular viscosity ν_0 to obtain the hydrodynamic relaxation times in the collision matrix Λ of the GLBE, as discussed in Sec. II.

To account for the damping of scales near the walls, following an earlier work [72], we have implemented the van Driest damping function [69]:

$$\Delta = \delta_x\left[1 - \exp\left(-\frac{z^+}{A^+}\right)\right] \tag{7}$$

where $z^+ = zu_*/\nu_0$ is the normal distance in wall units from the wall (u_* is the friction velocity related to the wall shear stress τ_w through $u_* = \sqrt{\tau_w/\rho}$), and A^+ is taken equal to 25 [72]. In this model, the friction velocity is generally unknown. To obtain the numerical value of this quantity, we used the logarithmic law due to von Kármán, which is given, for example, in [70]:

$$\frac{\langle U(z_g)\rangle}{u_*} - A\,\ell_n\left(\frac{z_g u_*}{\nu_0}\right) - B = 0, \qquad A = 2.5, \qquad B = 5.2 \tag{8}$$

where $\langle U(z_g)\rangle$ represents the mean velocity at a distance z_g from the wall. Equation (8), which is nonlinear, can be solved in a few iterations with the Newton–Raphson method to determine u_*. Note that very close to the wall in the viscous sublayer region, the velocity becomes proportional to the distance, and so a simple linear relation is instead used in this region. Although this approach obviously has some empiricism built in, such treatment for near-wall layers is common in computational fluid dynamics codes for LES, owing to its simplicity and computational efficiency. Indeed, such a procedure has recently been employed for LES of flows past cavities using a Navier–Stokes-based finite volume approach [27].

IV. Boundary Conditions

To solve the GLBE in Eqs. (2) and (3), suitable boundary conditions need to be specified. We employ the so-called interpolated bounceback scheme [73] for implementing the no-slip velocity conditions at the walls. It specifies the distribution functions for the incoming particle directions from the wall: $\bar{\alpha}$, where $\mathbf{e}_{\bar{\alpha}} = -\mathbf{e}_\alpha$, based on the near-wall postcollision information, and a factor q. Here, q represents the fractional distance of the wall from the near-wall lattice node in comparison with the lattice spacing δ_x. With linear interpolation of near-wall physics, we get [73]

$$f_{\bar{\alpha}}(\mathbf{x}, t+\delta_t) = 2q\tilde{f}_\alpha(\mathbf{x}, t) + (1-2q)\tilde{f}_\alpha(\mathbf{x} - \mathbf{e}_\alpha\delta_t, t), \qquad q < \tfrac{1}{2} \tag{9}$$

$$f_{\bar{\alpha}}(\mathbf{x}, t+\delta_t) = \frac{1}{2q}\tilde{f}_\alpha(\mathbf{x}, t) + \left(1 - \frac{1}{2q}\right)\tilde{f}_{\bar{\alpha}}(\mathbf{x}, t), \qquad q \geq \frac{1}{2} \tag{10}$$

When $q = \frac{1}{2}$, the preceding expressions reduce to the standard link-based bounceback scheme: that is,

$$f_{\bar{\alpha}}(\mathbf{x}, t+\delta_t) = \tilde{f}_\alpha(\mathbf{x}, t)$$

Because the cavity walls are straight surfaces, we choose $q = \frac{1}{2}$ in this work, which guarantees mass conservation. These boundary conditions are useful in accurately representing the profile of the boundary.

For an inflow boundary surface with a specified velocity $\mathbf{u}_{\text{in}}$, an extended link-bounceback scheme [74] that adds appropriate momentum to the particle populations is implemented:

$$f_{\bar{\alpha}}(\mathbf{x}, t+\delta_t) = \tilde{f}_\alpha(\mathbf{x}, t) + 2w_\alpha\rho_{\text{in}}\frac{\mathbf{e}_{\bar{\alpha}}\cdot\mathbf{u}_{\text{in}}}{c_s^2} \tag{11}$$

where w_α is a weighting factor. For outflow boundaries, an extrapolation method [75] is employed:

$$f_{\bar{\alpha}}(\mathbf{x}, t+\delta_t) = 2\tilde{f}_{\bar{\alpha}}(\mathbf{x}, t) - \tilde{f}_{\bar{\alpha}}(\mathbf{x} - \mathbf{e}_\alpha\delta_t, t) \tag{12}$$

where the equilibrium distribution in the collision step for the boundary lattice nodes are specified in terms of the no-gradient conditions for the macroscopic quantities.

V. Parallel Computing Strategy

One of the main advantages of the LBE is its natural amenability for implementation on parallel computers, making it particularly suitable for dealing with large problem sets. The explicit and essentially local nature of the computational algorithm of the GLBE [see Eqs. (2) and (3)] was exploited to parallelize the code using a domain decomposition strategy. The message-passing-interface library was used for the exchange of information between processors.

The parallelized GLBE code with the Smagorinsky SGS model was initially tested for speedup by performing LES of turbulent channel flow with a top free-slip surface at a shear Reynolds number Re_* of 180 based on channel half-height. The computational domain was discretized by employing $270 \times 135 \times 45$ grid nodes. A detailed description of the comparison of the turbulence statistics results with available data is presented in [66]. The code was tested for parallel performance by running on up to 16 processors on an IBM p690 cluster at the National Center for Supercomputing Applications (NCSA). Figure 2 shows the speedup for different numbers of processors. As may be expected, it shows that the GLBE code scales nearly linearly. All computations of cavity flows, which will be discussed in the following, were performed using a parallelized implementation of the GLBE on 8 processors of this computer cluster at NCSA.

VI. Results and Discussion

First, we briefly discuss the essential elements of the feedback-generated tones in cavity flows in different configurations, as proposed by Rossiter [4], before elaborating on the computational setup and results and their comparison with previous data. If L is the width of the cavity and U_c is the convection velocity of vortical structures generated from shear-layer instability (observations indicate $U_c = 0.4U_0$ to $0.6U_0$, where U_0 is the freestream velocity), the vortical structures travel across the cavity edges in time L/U_c. On the other hand, sound generated from unsteady impingement of vortices on the cavity trailing edge (a monopole source due to local mass flow rate variations) is radiated back upstream in time L/c_s, where c_s is the speed of sound, to the leading cavity edge, such that it reinforces the periodic vortical shedding of frequency f. This elegant

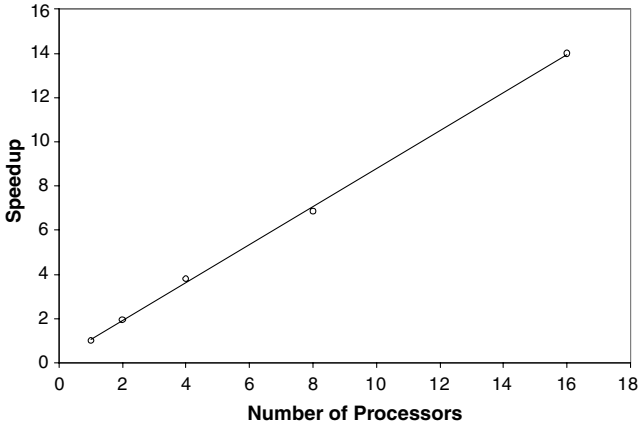

Fig. 2 Parallel performance of the GLBE implementation for turbulent channel flow simulation on a IBM p690 parallel cluster at NCSA.

model for feedback-flow-generated discrete tones leads to the following simple relation, the Rossiter formula [4]:

$$\frac{L}{U_c}+\frac{L}{c_s}=\frac{n}{f}, \qquad n=1,2,\ldots, \tag{13}$$

where n is the mode number. It may noted that the phenomenon of feedback-generated sound was first deduced in other contexts, such as in edge tones, somewhat earlier by Powell [76].

To match the predictions of expression (13) with experiments, it becomes necessary to take into account the phase lag β/f (β is a phase-lag factor) between the moments of acoustic pulse radiation and the vortical impingement at the trailing cavity edge, as well as those between the arrival of sound pulse at the leading cavity edge and the generation of new vortical structures. Thus, we have the modified Rossiter's equation given in terms of the Strouhal number (see, for example, Howe [15]):

$$St=\frac{fL}{U_0}=\frac{(n-\beta)}{[U_0/U_c+Ma/\sqrt{1+(\gamma-1)Ma^2/2}]}, \qquad n=1,2,\ldots, \tag{14}$$

where γ is the ratio of specific heats. This formula compares reasonably well with observations for shallow rectangular cavities (i.e., with $L/D>1$ and for $Ma>0.2$, $\beta\approx 0.25$, and $U_c/U=0.6$), where D is the depth of the cavity. For deep cavities, analytical models have been developed for flow/acoustic resonance based on vortex sound theory [15].

In the following, we performed wall-resolved 3-D LES of both deep and shallow cavities. That is, in each case, we employed 3 grid nodes to resolve the viscous sublayer and the use of a wall model is thereby avoided. We have considered a spacing of Δ^+ of about 4 in the bulk region and a spacing of Δ^+_{nw} of about 2 for the first grid node from the wall (resulting from the use of the halfway bounceback scheme). For the moderate Reynolds numbers considered in this paper, we have used at least 10 million grid nodes to resolve the domain for each case, which is at least twice as much considered in other studies for a similar range of Reynolds numbers (e.g., [27,30]). For example, in the case of shallow cavities, Gloerfelt et al. [27] used 5.37 million grid nodes (for $Re_D=48,600$) and Suponitsky et al. [30] employed 0.52 million grid nodes (for $Re_D=5000$), whereas in the present paper, we used 10.89 million grid nodes (for $Re_D=7000$). It may also be noted that the GLBE approach employed in our work has been assessed and validated for wall-resolved 3-D LES of a set of canonical wall-bounded flows, such as turbulent channel flow and turbulence-induced secondary flows in a square duct [66,77,78]. Although very recent studies have shown that the time-averaged mean fluid motion can become 3-D in cavities [24,29], we performed time and spatial averaging in the spanwise direction just to compare our results with other available data at moderate Reynolds numbers [27,30]. The computations were initially run for typically about $50T^*$, where T^* is the ratio of the width of the cavity and the freestream velocity, and the statistics of the fluid motion were collected by another additional run of about $100T^*$.

A. Flow Instabilities in a Deep Cavity with a Splitter Plate

Let us first consider a problem consisting of flow past a deep cavity with a splitter plate. This is one of the canonical computational aeroacoustics (CAA) problems specified in category 6 of the Third Computational Aeroacoustics Workshop on Benchmark Problems [79]. A schematic of the geometry of the cavity is shown in Fig. 3. The grid resolution is $900\times 110\times 250$ in the streamwise, spanwise, and wall-normal directions, respectively. The depth of the cavity D shown in Fig. 3 is resolved by 140 grid nodes, and the width of the cavity is related to the depth through the ratio $L/D=0.64$. The cavity consists of a splitter plate of length L_0 and thickness T_0, which

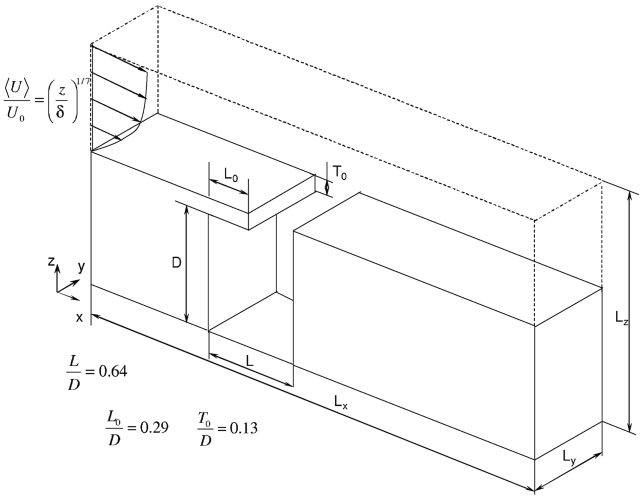

Fig. 3 Schematic representation of the geometry of a deep cavity with a splitter plate.

are related to the depth of the cavity by the ratios $L_0/D=0.29$ and $T_0/D=0.13$. These aspect ratios for the geometry correspond to those specified in [79]. The center of the opening of the cavity is placed roughly toward the center of the computational domain. The Reynolds number is defined here as $Re_D=U_0D/\nu_0=16,333$, where U_0 is the freestream velocity. The Mach number Ma based on the freestream velocity is taken to be 0.24. The Reynolds number used here is well within the range of that employed by 3-D LES computations performed using finite difference methods with full near-wall resolution (e.g., [30]).

At the inlet, as stipulated in the statement of the benchmark problem [79], a one-seventh power-law profile is used for the mean streamwise velocity profile:

$$\frac{u}{U_0}=\left(\frac{z}{\delta}\right)^{1/7} \tag{15}$$

where δ is the boundary-layer thickness. Following a recent 3-D LES study of cavity flows [30], a random inflow perturbation, with maximum amplitude of 10% of the local mean velocity, is applied to trigger the development of three-dimensional turbulence. It may be noted that for the generation of tones in cavities, self-sustained oscillations need to occur, which depends on upstream flow conditions and the geometric details of the cavity.

In the cavity flow measurements and visualization by Sarohia [7], it was found that the thickness of the boundary layer δ, the width of the cavity L, and the freestream velocity U_0 should satisfy the following criteria for tones to occur: $\delta/D<0.5$ and $(L/\delta)\sqrt{Re_D(\delta/D)}>290$. Also, in their DNS studies of cavity flows, Colonius et al. [21] found that L/θ, where θ is the momentum thickness, must be greater than a certain value that depends on the Reynolds number and Mach number used (note that $\theta=n/[(n+1)(n+2)]\delta$, for a general power-law velocity distribution $u/U_0=(z/\delta)^{1/n}$) [70]. In other words, in relative terms, the boundary layer should not be too thick for undamped flow oscillations to occur. Although these criteria are obtained for unstable laminar flows in shallow cavities, it is nevertheless useful in guiding the choice of parameters for the present work. The boundary-layer thickness δ is chosen such that $(L/\delta)\sqrt{Re_D(\delta/D)}\approx 435$ and $L/\theta=185.6$, which, as will be shown in the following, is sufficient to ensure self-sustained oscillations.

In what follows, quantities will be expressed in lattice units; that is, the length scales are normalized by the lattice spacing δ_x and fluid flow velocities are normalized by the particle velocity c (and hence time scales are normalized by δ_x/c). In our computations, we choose the freestream velocity $U_0=0.14$ and molecular viscosity of the fluid $\nu_0=0.0012$, and so the Reynolds number based on the depth of the cavity Re_D is 16, 333.

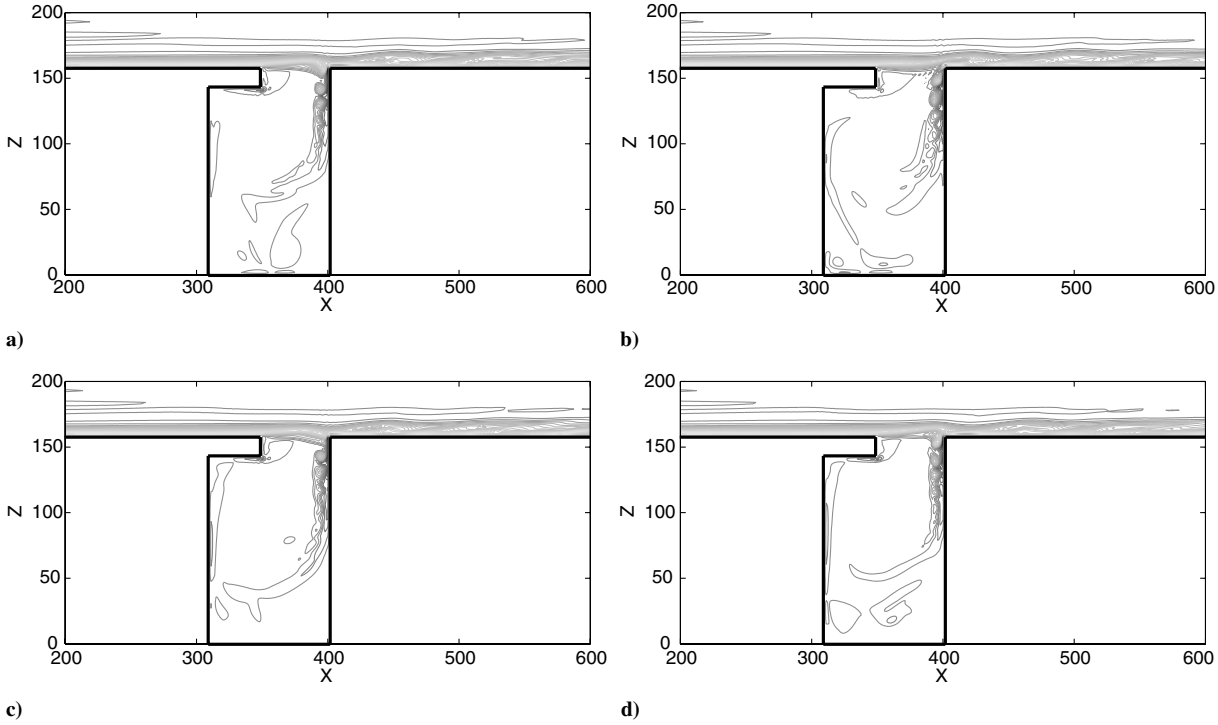

Fig. 4 Instantaneous spanwise vorticity contours in the midspanwise plane (i.e., at $y = 55$ in the near field of the deep cavity with a splitter plate at different instants for $Re_D = 16,333$, $L/\theta = 185.6$, and $Ma = 0.24$): a) $t = 85,000$, b) $t = 95,000$, c) $t = 110,000$, and d) $t = 125,000$.

Figure 4 shows the computed instantaneous spanwise vorticity contours at the midspanwise plane in the near field of the cavity at a few different times. It is apparent that as the unstable vortical structures impinge on the downstream cavity edge and wall, some part of them falls into the cavity, whereas the rest continue to be convected downstream of the trailing edge of the cavity, along the outside flat surface. The falling vortices within the cavity roll down along the downstream cavity edge, setting up a recirculating flow region.

The time traces of the normal velocity W at three different locations around the cavity opening are shown in Figs. 5–7. See Fig. 4 for details on the coordinate locations in these figures. It is evident that self-sustained flow oscillations with a discrete frequency occur at these locations. The spectral component of the normal velocity is obtained by taking a discrete Fourier transform (DFT) and the results in the preceding three figures are presented in terms of Strouhal number $St = fL_{\text{cm}}/U_0$, where L_{cm} is the width of the cavity mouth. The computed value is $St = 0.344$.

It may be noted that recent experiments based on laser–Doppler velocimetry for flow over a deep cavity, albeit with somewhat different aspect ratio and at higher subsonic Mach numbers and Reynolds numbers than considered here, revealed regular self-sustained oscillations with a periodic organization of shear layer over the cavity mouth with a dominant first mode [10]. On the other hand, data are available for a setup with geometric aspect ratios similar to those considered here from the experiments of Henderson [79]. The measurement data [79] for the resonant frequency in terms of Strouhal number at different Mach numbers are given in Table 1, which also provides data from some computational studies for this problem.

The values are in the range 0.319 to 0.369. A DNS study based on the dispersion-rate-preserving (DRP) scheme by Kurbatskii and Tam [80] found $St = 0.344$. Unsteady DES based on the Spalart–Allmaras model [32] have yielded Strouhal numbers of 0.36 and 0.33 for the lowest normal mode [81]. Also, computations based on an acoustic/viscous splitting procedure [83] yield $St = 0.377$ [82]. It is evident that the GLBE results for the flow/acoustic resonant frequency are in very good agreement with previous measurements and computations. Moreover, inspection of a set of instantaneous vorticity contours in the near field of the cavity provided in some of

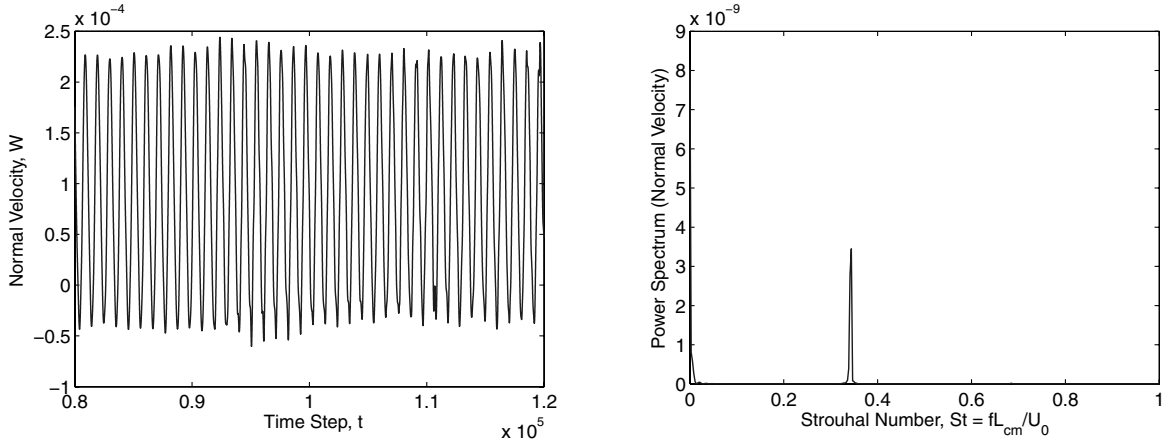

Fig. 5 Time trace of normal velocity W for $Re_D = 16,333$, $L/\theta = 185.6$, and $Ma = 0.24$ (left); corresponding power spectrum of normal velocity in terms of Strouhal number in the vicinity of the mouth of the deep cavity at $x = 300$ and $z = 200$ (right).

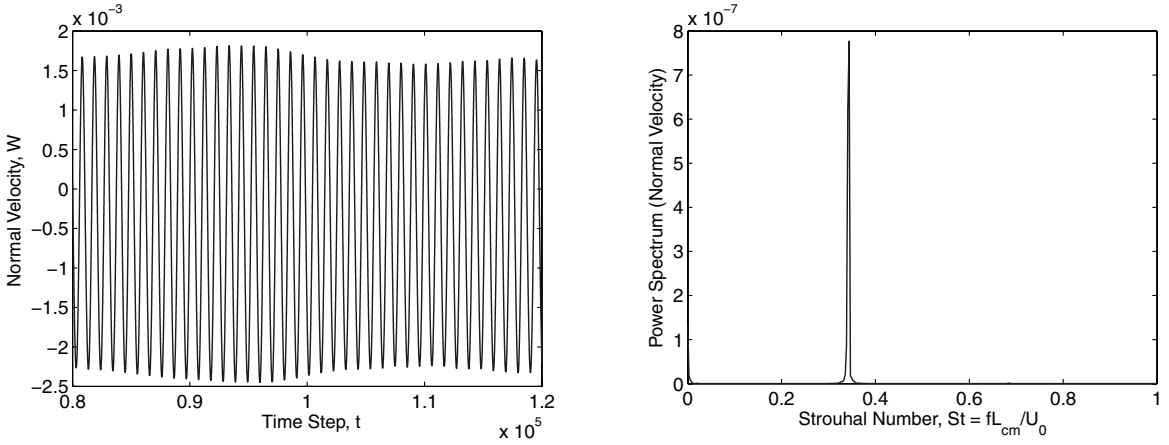

Fig. 6 Time trace of normal velocity W for $Re_D = 16,333$, $L/\theta = 185.6$, and $Ma = 0.24$ (left); corresponding power spectrum of normal velocity in terms of Strouhal number in the vicinity of the mouth of the deep cavity at $x = 360$ and $z = 170$ (right).

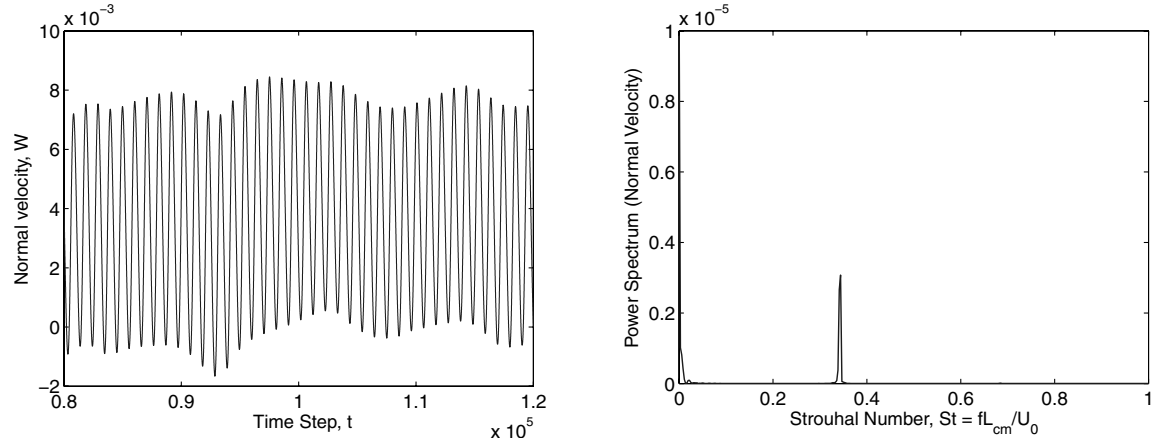

Fig. 7 Time trace of normal velocity W for $Re_D = 16,333$, $L/\theta = 185.6$, and $Ma = 0.24$ (left); corresponding power spectrum of normal velocity in terms of Strouhal number in the vicinity of the mouth of the deep cavity at $x = 375$ and $z = 150$ (right).

these computational studies show that they are themselves consistent with each other and with this study.

In contrast to the shallow cavities, partly due to a shorter opening in deep cavities, the separated flow can no longer reattach to the cavity floor. As a result, some vortical structures closer to the cavity base become captive and isolated from the main flow, as presented in Fig. 8, which shows the mean streamlines in the near field of the cavity. This figure shows the presence of large-scale upper and lower vortices along with smaller corner vortices. Such features are generally absent in shallow cavities. It may be noted that some earlier visualization and measurement studies in deep cavities have indeed observed such multiple large-scale vortical structures accompanied by recirculation regions [2,3,11].

Table 1 Comparison of flow-resonant frequency from a deep cavity with splitter plate in terms of Strouhal number

Data source	Strouhal number ($St = fL_{cm}/U_0$)
Experiments (thin boundary layer) [79]	
$Ma = 0.06$	0.336
$Ma = 0.09$	0.369
$Ma = 0.12$	0.319
$Ma = 0.18$	0.334
DNS/DRP scheme [80]	0.343
DES [81]	
Laminar	0.360
Turbulent	0.330
Acoustic/viscous splitting procedure [82]	0.377
GLBE/LES (this study)	0.344

B. Flow Instabilities in a Shallow Cavity

We now consider a shallow cavity with a width-to-depth ratio of $L/D = 2.5$. The width is resolved by 150 grid nodes, and the computational domain is resolved by $550 \times 110 \times 180$ grid nodes. The Reynolds number Re_D based on the depth of the cavity is 7000 and the freestream Mach number Ma is 0.24. The inlet velocity is specified in a similar manner to that in the previous section. The boundary-layer thickness is chosen to be relatively thin such that $L/\theta = 193.3$ and $(L/\delta)\sqrt{Re_D(\delta/D)} \approx 573$, which we find a posteriori to be sufficient to ensure self-sustained oscillations. Figure 9 shows the instantaneous spanwise vorticity contours at a few different times. Kelvin–Helmholtz instability of the shear layer is clearly evident in this case, with greater lateral motions of the vortical structures, as compared with the deep-cavity case considered earlier. Moreover, larger vortices convect along the wall surface outside of the cavity than before.

From the point of view of stability theory of near parallel flows, the feedback sound mechanism in the absence of external forcing can be viewed as the convective Kelvin–Helmholtz instability of the vortical structures comprising the shear-layer region leading to globally unstable flow (i.e., upstream propagation of self-sustained flow instabilities [84,85] by the acoustic wave propagation [23]). The shear-layer profile, in terms of the mean streamwise velocity at different stations in cavity opening, presented in Fig. 10, shows deviations from the hyperbolic tangent profile, with significant backflow, which was also observed in the recent 3-D LES computations [30]. It was shown by Huerre and Monkewitz [85] that if the backflow deviations of hyperbolic tangent profile for velocity are greater than 13.6%, the flow is absolutely unstable (i.e., upstream propagation of energy growth of instability). The computations

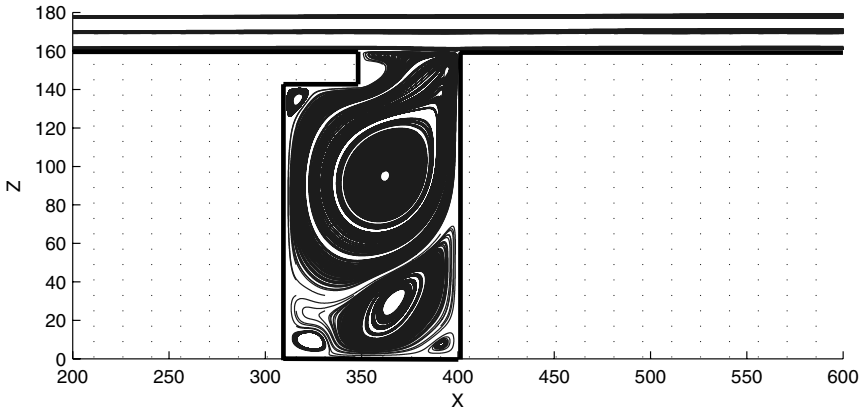

Fig. 8 Mean streamlines in the near field of the deep cavity with a splitter plate for $Re_D = 16,333$, $L/\theta = 185.6$, and $Ma = 0.24$.

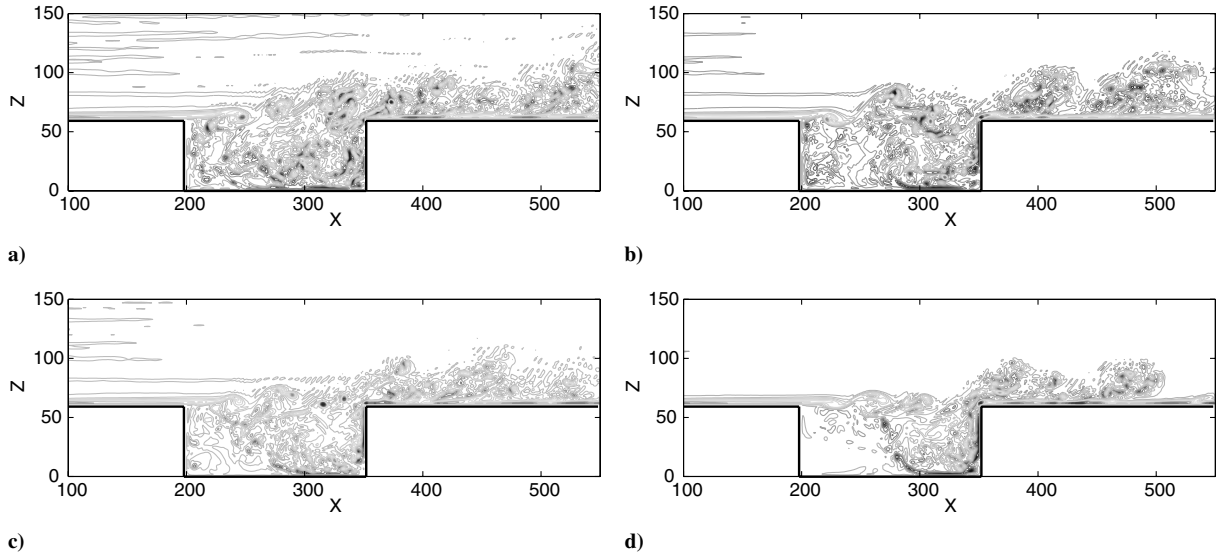

Fig. 9 Instantaneous spanwise vorticity contours in the midspanwise plane (i.e., at $y = 55$ in the near field of the shallow cavity at different instants for $Re_D = 7000$, $L/\theta = 193.3$, and $Ma = 0.24$): a) $t = 65,000$, b) $t = 70,000$, c $t = 75,000$, and d) $t = 80,000$.

presented here seem to be consistent with this earlier finding and in this sense, with the acoustic feedback mechanism in place, the flow oscillations may be considered to be due to global instability.

To quantify the oscillations for this case, we present the time trace of the normal velocity W at two different locations around the cavity opening in Figs. 11 and 12. The flow does indeed appear to maintain

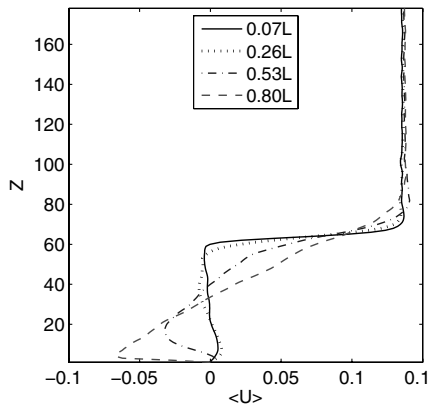

Fig. 10 Mean streamwise velocity profiles at different locations measured from the leading edge of the shallow cavity, showing shear-layer development for $Re_D = 7000$, $L/\theta = 193.3$, and $Ma = 0.24$.

self-sustained oscillations and the characteristic oscillation frequency is obtained by taking the power spectra of the velocities which are also shown in the preceding two figures. The Strouhal number based on cavity width L is found to be about 0.84. As noted earlier, the modified Rossiter formula (14) is applicable for shallow cavities when $Ma > 0.2$.

When $\gamma = 1$ in Eq. (14), it simplifies to

$$St_n = \frac{f_n L}{U_0} = \frac{n - \beta}{(U_0/U_c) + Ma}$$

Considering typical values of the phase-lag factor and vortical convection speed (i.e., $\beta = 0.25$ and $U_c/U_0 = 0.60$), we find the Strouhal numbers of the first two modes of oscillations to be $St_1 = 0.39$ and $St_2 = 0.91$, respectively. It is thus apparent that the present computations correspond to the second mode of oscillations. It was observed by Sarohia [7] in shallow-cavity flow experiments that as the boundary layer became thinner (i.e., as L/θ increases when all other controlling parameters are unchanged), the flow oscillations switch from mode 1 to mode 2. At relatively larger L/θ values, the observed Strouhal number for the second mode is in the range of $St_2 = 0.80$–0.95. Moreover, a recent 3-D LES computation of shallow cavity flows found $St_2 = 0.83$–1.0, depending on the SGS model used [30], and another one found $St_2 = 0.75$, albeit at high subsonic Mach numbers [27]. Thus, we find that the GLBE is also able to reproduce the dominant frequency in shallow-cavity flows reasonably well.

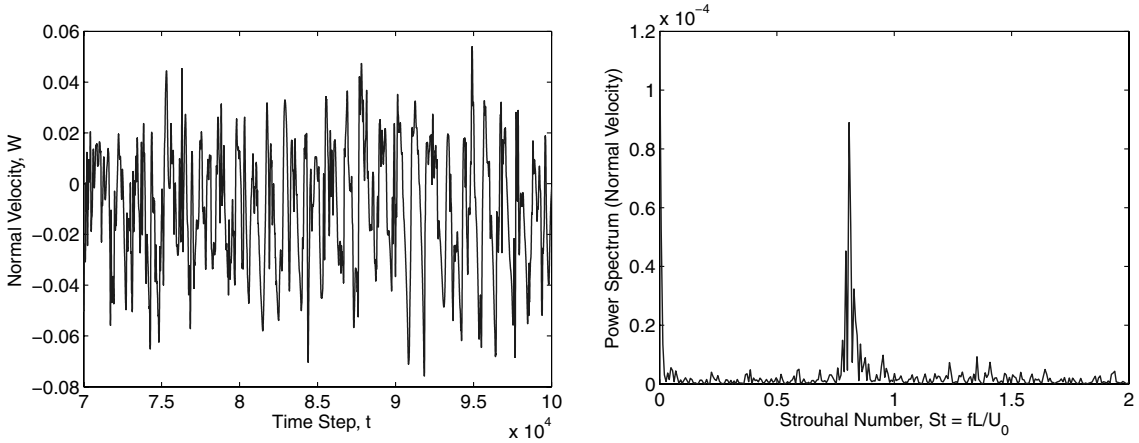

Fig. 11 Time trace of normal velocity W for $Re_D = 7000, L/\theta = 193.3$, and $Ma = 0.24$ (left); corresponding power spectrum of normal velocity in terms of Strouhal number in the vicinity of the mouth of the deep cavity at $x = 330$ and $z = 60$ (right).

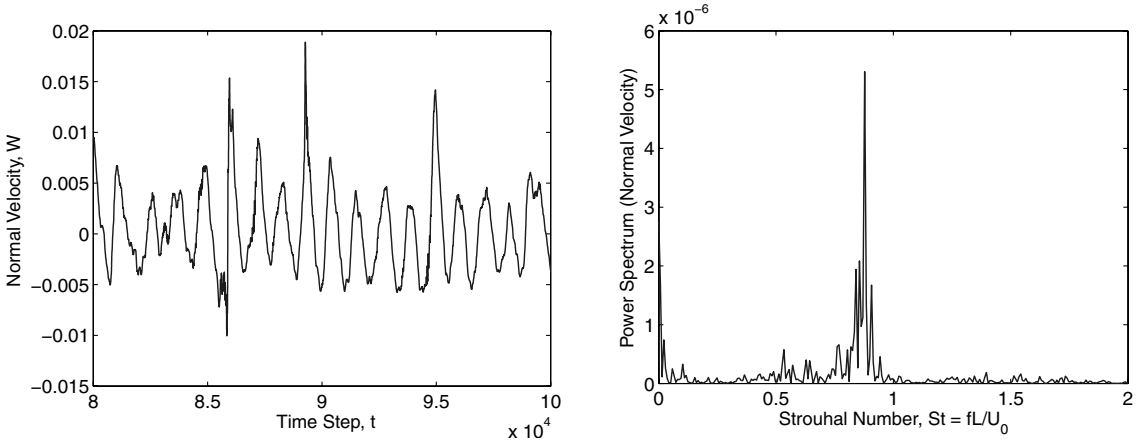

Fig. 12 Time trace of normal velocity W, for $Re_D = 7000, L/\theta = 193.3$, and $Ma = 0.24$ (left); corresponding power spectrum of normal velocity in terms of Strouhal number in the vicinity of the mouth of the deep cavity at $x = 350$ and $z = 100$ (right).

An important test of the novel numerical approach employed here is whether it can also predict the intensities of flow oscillations at different locations in the cavity-mouth region and which can reasonably be matched by any independently available previous data. It may be noted that experimental data for different cavity configurations are available at high Re_D [i.e., $\mathcal{O}(10^6)$]. Although such conditions can be matched using wall models [28,29], they are beyond the reach of any wall-resolved LES, due to computational constraints. On the other hand, very recently, 3-D DNS has been carried out for $Re_D \sim \mathcal{O}(10^3)$ [24]. However, their main focus was on the investigations of flow stability characteristics under a variety of conditions, and detailed data on the intensities of velocity fluctuations at different locations in the cavity region are not available for comparison. At the same time, a few 3-D LES studies were carried out recently for moderate $Re_D \sim \mathcal{O}(10^3)$ [27,30], which are within the range considered here. In particular, Gloerfelt et al. [27] provide detailed data of the root-mean-square velocity fluctuations in the cavity opening, with which we make comparisons in what follows.

The computed root-mean-square (rms) streamwise, spanwise, and wall-normal velocity fluctuations within the mixing layer developing between the leading and trailing edges of the cavity at three different stations ($x/L = 0.3, 0.5, 0.9$) are shown in Figs. 13–15, respectively. The data by Gloerfelt et al. [27] are provided in symbols for comparison. It can be seen that fluctuations at a relatively high velocity are found within the cavity shear-layer region, with peaks at about 20% of the freestream velocity. Moreover, all three components have significant contributions, which is an indication of the three-dimensional and turbulent nature of the flow over the cavity. It is evident that the detailed structure of the computed rms velocity fluctuations are in reasonably good agreement with the available data. In particular, the GLBE solutions for the spanwise and wall-normal intensities closely agree with the Gloerfelt et al. [27] results. Although the computed streamwise intensity profiles are still qualitatively similar to the Gloerfelt et al. results, the peaks are underpredicted, particularly near the leading edge of the cavity. This could be due to various factors, including the fact that different approaches were employed to implement inflow perturbations, that lead to the Kelvin–Helmholtz instability in the shear-layer region. Moreover, the Reynolds number and Mach number considered by Gloerfelt et al. are higher than those employed here. Because the computed results are in reasonably good agreement with a priori results using a completely different numerical approach, these comparisons constitute an independent verification of the applicability of our approach.

The results for the Reynolds stress $\langle -u'w' \rangle$ are not provided by Gloerfelt et al. [27]. Nevertheless, we present the computed structure of the Reynolds stress at different stations in the cavity opening region in Fig. 16. Its nondimensional peak value is found to vary between about 0.01 and 0.03. Although other studies were performed at much higher Reynolds numbers [28], nevertheless, our computed range is similar to those reported by them.

The three-dimensionality of the flow becomes evident from an instantaneous isosurface plot of spanwise vorticity in the near field of the cavity presented in Fig. 17, which shows intense mixing of vortical structures in the cavity opening. It may also be noted that the mean streamlines in the near field of the shallow cavity shown in Fig. 18 contrast significantly with those for the deep cavity (Fig. 8),

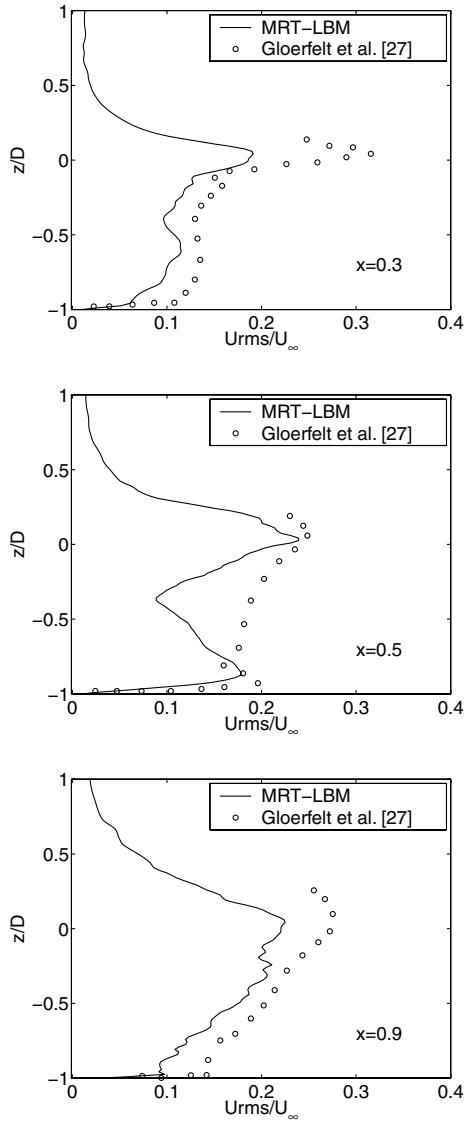

Fig. 13 Root-mean-square streamwise velocity fluctuations at different locations ($x/L = 0.3, 0.5, 0.9$) measured from the leading edge of the shallow cavity for $Re_D = 7000$, $L/\theta = 193.3$, and $Ma = 0.24$.

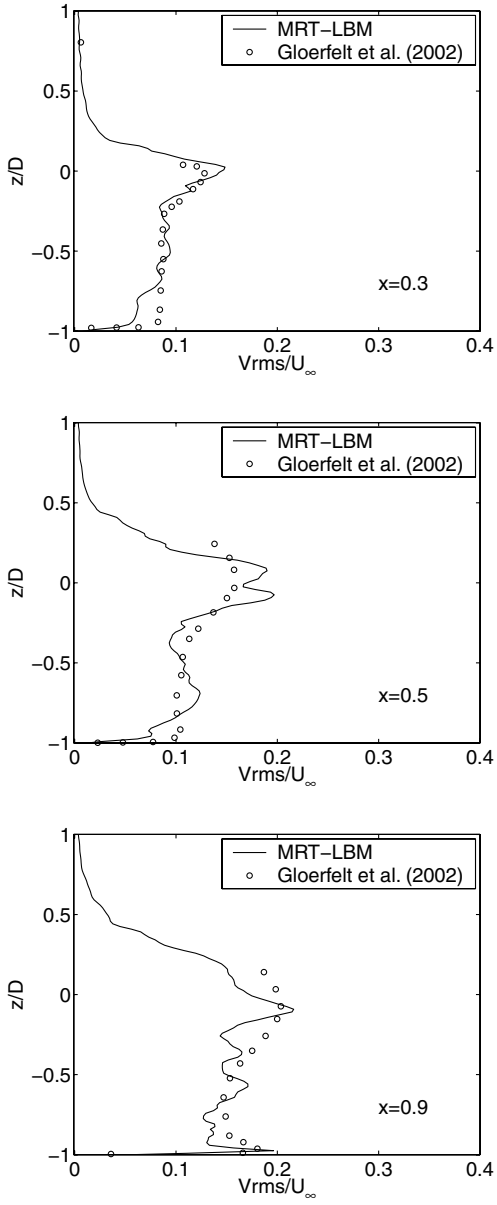

Fig. 14 Root-mean-square spanwise velocity fluctuations at different locations ($x/L = 0.3, 0.5, 0.9$) measured from the leading edge of the shallow cavity for $Re_D = 7000$, $L/\theta = 193.3$, and $Ma = 0.24$.

with no trapping of large-scale vortical structures in the former case. In particular, Fig. 18 shows the presence of main and secondary vortices along with smaller corner vortices. In fact, such features are characteristic of shallow-cavity flows, as was observed in recent flow visualization experiments [11] and computations using other methods [23,30].

C. Flow Instabilities in a Deep Cavity

We considered flow past a deep cavity with a splitter plate in Sec. VI.A. In this section, let us consider the effect of removing the splitter plate, which effectively widens the mouth of the cavity, but keeps other factors the same as before. Such a simplified problem admits modal analysis by analytical methods [86] and was considered in a numerical simulation by Shieh and Morris [81]. As before, the computational domain was resolved by $900 \times 110 \times 150$ grid nodes, but maintains the same flow parameters and conditions as discussed in Sec. VI.A.

Figure 19 shows the computed instantaneous spanwise vorticity contours at different times in the near field of the cavity. In contrast to Fig. 4, Fig. 19 shows a more pronounced effect of shear-layer instability in the cavity-mouth region, showing shedding of smaller vortices upon their impingement at the downstream cavity edge, setting up recirculating patterns.

The temporal variation of the normal velocity at the location $x = 375$ and $z = 200$ is shown in Fig. 20. Strong, self-sustained, resonating, oscillatory fluid motion can be clearly observed with multiple discrete frequencies. Through a DFT, the primary mode of oscillation is deduced to occur at a frequency corresponding to a Strouhal number of 0.72. This compares reasonably well with the analytical solution for the frequency of the lowest mode in a rectangular cavity obtained using a mode analysis by Tam [86], which gives a value of 0.68. Moreover, the computations by Shieh and Morris [81] yielded Strouhal numbers of 0.64 and 0.58 for laminar and turbulent conditions, respectively. The second mode is found to occur at a considerably higher frequency, with a Strouhal number of about 1.36. Shieh and Morris also observed such higher-frequency modes in their computations. Mean streamlines for the present case are shown in Fig. 21. Comparison of Figs. 8 and 21 show significant differences in the flow patterns. In particular, the presence of a splitter plate in a deep cavity appears to somewhat squish and skew the lower vortical structures, whereas they are more evenly distributed when the splitter plate is removed.

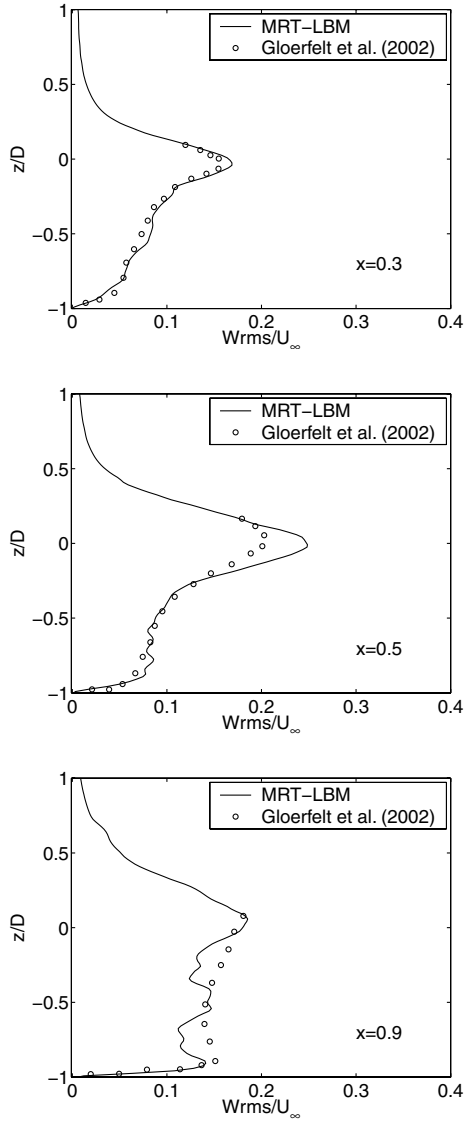

Fig. 15 Root-mean-square wall-normal velocity fluctuations at different locations ($x/L = 0.3, 0.5, 0.9$) measured from the leading edge of the shallow cavity for $Re_D = 7000$, $L/\theta = 193.3$, and $Ma = 0.24$.

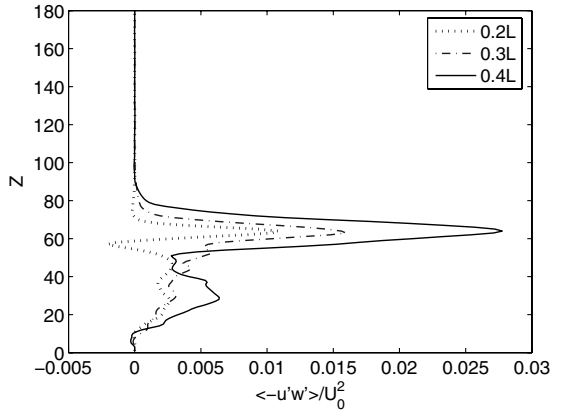

Fig. 16 Reynolds stress $\langle -u'w' \rangle$ at different locations measured from the leading edge of the shallow cavity for $Re_D = 7000$, $L/\theta = 193.3$, and $Ma = 0.24$.

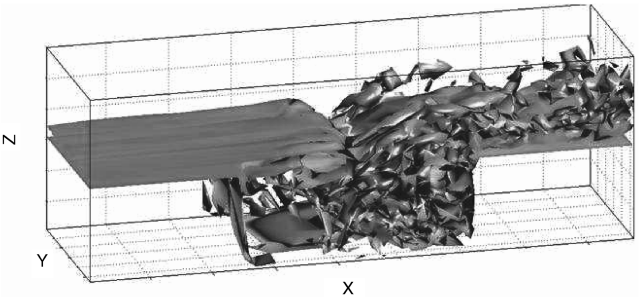

Fig. 17 Instantaneous isosurfaces of spanwise vorticity in the near field of the shallow cavity for $Re_D = 7000$, $L/\theta = 193.3$, and $Ma = 0.24$.

VII. Conclusions

Large-eddy simulations of subsonic flow past cavities at moderate Reynolds numbers ($Re \sim \mathcal{O}(10^4)$) are performed to investigate flow instabilities and oscillations using a numerical technique based on a recently developed form of the generalized lattice-Boltzmann equation. In this regard, the Smagorinsky subgrid-scale model modulated by the van Driest damping function near walls is employed.

It is found that the flow in a shallow cavity at a Reynolds number based on cavity width of 17,500 and aspect ratio of $L/D = 2.5$ exhibits Kelvin–Helmholtz shear-layer instability, maintaining a globally unstable state. The flow oscillations are found to correspond to the second Rossiter mode, with a Strouhal number of 0.84, which is consistent with a previous 3-D study based on solution of the filtered Navier–Stokes equations. Fully three-dimensional velocity fluctuations are observed in the cavity-mouth region. The detailed structure of computed root-mean-square velocity fluctuations are found to be in reasonable agreement with previous computational results obtained using a different computational approach. The mean flowfields showed the presence of two large vortical structures in the cavity, one occupying the upstream region and the other in the downstream portion.

For the case of flow past a deep cavity with a splitter plate covering the upstream part of the cavity at a Reynolds number based on cavity width of 10,450, flow-resonant oscillations with a nondimensional frequency or Strouhal number of 0.34 are observed, which is in very good agreement with previous data from various sources. The mean flowfield is characterized by the presence of a recirculation region in the upper part of the cavity, with a counter-rotating vortex below and some smaller vortices in the corners, which are markedly different from those of the shallow cavity. When the splitter plate is removed

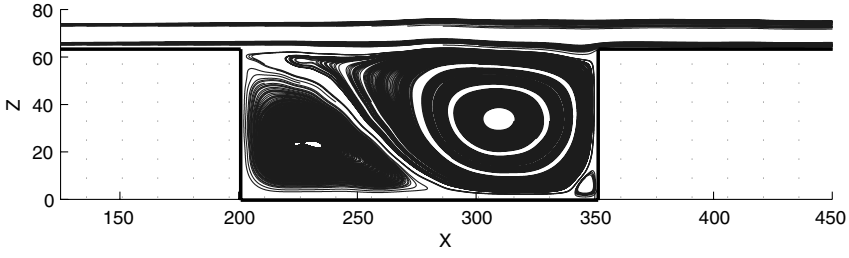

Fig. 18 Mean streamlines in the near field of the shallow cavity for $Re_D = 7000$, $L/\theta = 193.3$, and $Ma = 0.24$.

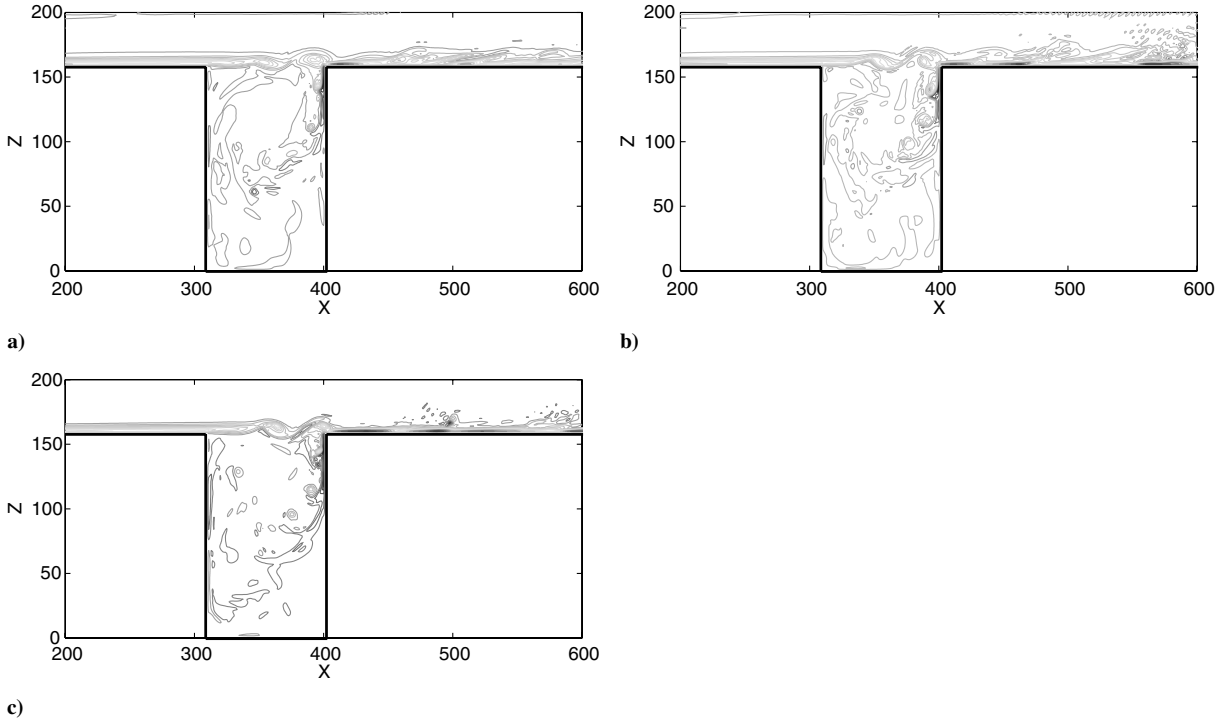

Fig. 19 Instantaneous spanwise vorticity contours in the midspanwise plane (i.e., at $y = 55$ in the near field of the deep cavity at different instants for $Re_D = 16,333$, $L/\theta = 185.6$, and $Ma = 0.24$): a) $t = 90,000$, b) $t = 100,000$, c) $t = 110,000$.

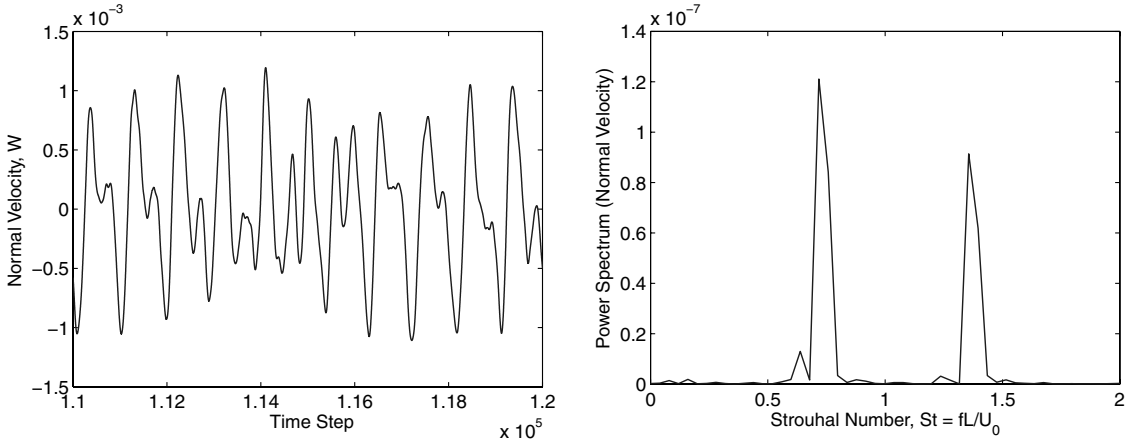

Fig. 20 Time trace of normal velocity W for $Re_D = 16,333$, $L/\theta = 185.6$, and $Ma = 0.24$ (left); corresponding power spectrum of normal velocity in terms of Strouhal number, based on cavity opening width L_{cm} and freestream velocity U_0, in the vicinity of the mouth of the deep cavity at $x = 375$ and $z = 200$ (right).

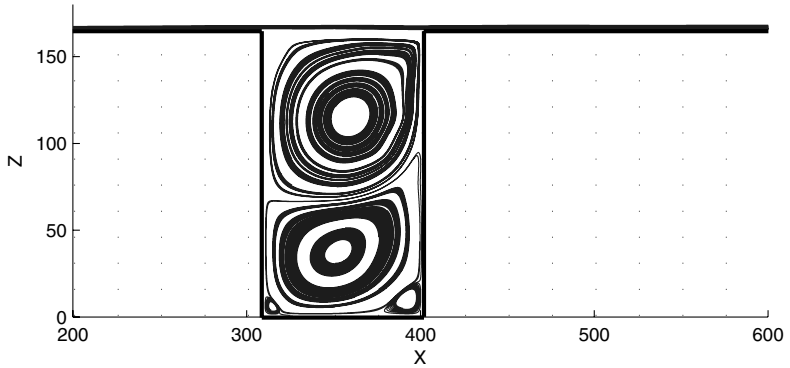

Fig. 21 Mean streamlines in the near field of the deep cavity for $Re_D = 16,333$, $L/\theta = 185.6$, and $Ma = 0.24$.

from the deep cavity, the flow is found to oscillate with a higher frequency, corresponding to a Strouhal number of 0.72, in good agreement with other simulation results. Moreover, a secondary mode of oscillation is also noticed for this configuration.

These findings suggest that the recent formulation of the lattice-Boltzmann equation based on multiple relaxation times used here provides an accurate approach for large-eddy simulation of flows and instabilities, with an ability to reproduce time-dependent complex flow characteristics. Because of the ease of representation of complex boundary shapes and its excellent parallel scalability, it appears to be promising approach for investigations of a wider class of problems.

Appendix: Moments, Equilibrium Moments, Moment Projections of Source Terms, and Strain-Rate Tensor

The components of the various elements in the moments for the D3Q19 lattice are as follows [59]:

$$\hat{f}_0 = \rho, \quad \hat{f}_1 = e, \quad \hat{f}_2 = e^2, \quad \hat{f}_3 = j_x$$
$$\hat{f}_4 = q_x, \quad \hat{f}_5 = j_y, \quad \hat{f}_6 = q_y, \quad \hat{f}_7 = j_z$$
$$\hat{f}_8 = q_z, \quad \hat{f}_9 = 3p_{xx}, \quad \hat{f}_{10} = 3\pi_{xx}, \quad \hat{f}_{11} = p_{ww}$$
$$\hat{f}_{12} = \pi_{ww}, \quad \hat{f}_{13} = p_{xy}, \quad \hat{f}_{14} = p_{yz}, \quad \hat{f}_{15} = p_{xz}$$
$$\hat{f}_{16} = m_x, \quad \hat{f}_{17} = m_y, \quad \hat{f}_{18} = m_z$$

where ρ is the density; e and e^2 represent kinetic energy that is independent of density and square of energy, respectively; j_x, j_y and j_z are the components of the momentum (i.e., $j_x = \rho u_x$, $j_y = \rho u_y$, and $j_z = \rho u_z$); q_x, q_y, and q_z are the components of the energy flux; and p_{xx}, p_{xy}, p_{yz}, and p_{xz} are the components of the symmetric traceless viscous stress tensor. The other two normal components of the viscous stress tensor, p_{yy} and p_{zz}, can be constructed from p_{xx} and p_{ww}, where $p_{ww} = p_{yy} - p_{zz}$. Other moments include π_{xx}, π_{ww}, m_x, m_y, and m_z. The first two of these moments have the same symmetry as the diagonal part of the traceless viscous tensor p_{ij}, and the last three vectors are parts of a third rank tensor, with the symmetry of $j_k p_{mn}$.

The corresponding components of the equilibrium moments, which are functions of conserved moments (i.e., density ρ and momentum $\mathbf{j}$) are as follows [59]:

$$\hat{f}_0^{\mathrm{eq}} = \rho, \quad \hat{f}_1^{\mathrm{eq}} \equiv e^{\mathrm{eq}} = -11\rho + 19\frac{\mathbf{j}\cdot\mathbf{j}}{\rho}$$
$$\hat{f}_2^{\mathrm{eq}} \equiv e^{2,\mathrm{eq}} = 3\rho - \frac{11}{2}\frac{\mathbf{j}\cdot\mathbf{j}}{\rho}, \quad \hat{f}_3^{\mathrm{eq}} = j_x$$
$$\hat{f}_4^{\mathrm{eq}} \equiv q_x^{\mathrm{eq}} = -\frac{2}{3}j_x, \quad \hat{f}_5^{\mathrm{eq}} = j_y, \quad \hat{f}_6^{\mathrm{eq}} \equiv q_y^{\mathrm{eq}} = -\frac{2}{3}j_y$$
$$\hat{f}_7^{\mathrm{eq}} = j_z, \quad \hat{f}_8^{\mathrm{eq}} \equiv q_z^{\mathrm{eq}} = -\frac{2}{3}j_z$$
$$\hat{f}_9^{\mathrm{eq}} \equiv 3p_{xx}^{\mathrm{eq}} = \frac{[3j_x^2 - \mathbf{j}\cdot\mathbf{j}]}{\rho}, \quad \hat{f}_{10}^{\mathrm{eq}} \equiv 3\pi_{xx}^{\mathrm{eq}} = 3\left(-\frac{1}{2}p_{xx}^{\mathrm{eq}}\right)$$
$$\hat{f}_{11}^{\mathrm{eq}} \equiv p_{ww}^{\mathrm{eq}} = \frac{[j_y^2 - j_z^2]}{\rho}, \quad \hat{f}_{12}^{\mathrm{eq}} \equiv \pi_{ww}^{\mathrm{eq}} = -\frac{1}{2}p_{ww}^{\mathrm{eq}},$$
$$\hat{f}_{13}^{\mathrm{eq}} \equiv p_{xy}^{\mathrm{eq}} = \frac{j_x j_y}{\rho}, \quad \hat{f}_{14}^{\mathrm{eq}} \equiv p_{yz}^{\mathrm{eq}} = \frac{j_y j_z}{\rho}$$
$$\hat{f}_{15}^{\mathrm{eq}} \equiv p_{xz}^{\mathrm{eq}} = \frac{j_x j_z}{\rho}, \quad \hat{f}_{16}^{\mathrm{eq}} = 0, \quad \hat{f}_{17}^{\mathrm{eq}} = 0, \quad \hat{f}_{18}^{\mathrm{eq}} = 0$$

The components of the source terms in moment space are functions of external force $\mathbf{F}$ and velocity fields $\mathbf{u}$, respectively, as follows [66]:

$$\hat{S}_0 = 0, \quad \hat{S}_1 = 38(F_x u_x + F_y u_y + F_z u_z)$$
$$\hat{S}_2 = -11(F_x u_x + F_y u_y + F_z u_z), \quad \hat{S}_3 = F_x$$
$$\hat{S}_4 = -\tfrac{2}{3}F_x, \quad \hat{S}_5 = F_y, \quad \hat{S}_6 = -\tfrac{2}{3}F_y, \quad \hat{S}_7 = F_z$$
$$\hat{S}_8 = -\tfrac{2}{3}F_z, \quad \hat{S}_9 = 2(2F_x u_x - F_y u_y - F_z u_z)$$
$$\hat{S}_{10} = -(2F_x u_x - F_y u_y - F_z u_z), \quad \hat{S}_{11} = 2(F_y u_y - F_z u_z)$$
$$\hat{S}_{12} = -(F_y u_y - F_z u_z), \quad \hat{S}_{13} = (F_x u_y + F_y u_x)$$
$$\hat{S}_{14} = (F_y u_z + F_z u_y), \quad \hat{S}_{15} = (F_x u_z + F_z u_x)$$
$$\hat{S}_{16} = 0, \quad \hat{S}_{17} = 0, \quad \hat{S}_{18} = 0$$

The components of the strain-rate tensor used in SGS turbulence models can be written explicitly in terms of nonequilibrium moments augmented by moment projections of source terms as [66]

$$S_{xx} \approx -\frac{1}{38\rho}\left[s_1\hat{h}_1^{(\mathrm{neq})} + 19s_9\hat{h}_9^{(\mathrm{neq})}\right] \tag{A1}$$

$$S_{yy} \approx -\frac{1}{76\rho}\left[2s_1\hat{h}_1^{(\mathrm{neq})} - 19\left(s_9\hat{h}_9^{(\mathrm{neq})} - 3s_{11}\hat{h}_{11}^{(\mathrm{neq})}\right)\right] \tag{A2}$$

$$S_{zz} \approx -\frac{1}{76\rho}\left[2s_1\hat{h}_1^{(\mathrm{neq})} - 19\left(s_9\hat{h}_9^{(\mathrm{neq})} + 3s_{11}\hat{h}_{11}^{(\mathrm{neq})}\right)\right] \tag{A3}$$

$$S_{xy} \approx -\frac{3}{2\rho}s_{13}\hat{h}_{13}^{(\mathrm{neq})} \tag{A4}$$

$$S_{yz} \approx -\frac{3}{2\rho}s_{14}\hat{h}_{14}^{(\mathrm{neq})} \tag{A5}$$

$$S_{xz} \approx -\frac{3}{2\rho}s_{15}\hat{h}_{15}^{(\mathrm{neq})} \tag{A6}$$

where

$$\hat{h}_\alpha^{(\mathrm{neq})} = \hat{f}_\alpha - \hat{f}_\alpha^{\mathrm{eq}} + \tfrac{1}{2}\hat{S}_\alpha, \qquad \alpha \in \{1, 9, 11, 13, 14, 15\} \tag{A7}$$

where $\hat{f}_\alpha$, $\hat{f}_\alpha^{\mathrm{eq}}$, and $\hat{S}_\alpha$ are components of moments, their local equilibria, and moment projections of source terms due to external forces, respectively, which are given previously, and s_α are elements of the collision matrix $\Lambda = \mathrm{diag}(s_0, s_1, \ldots, s_{18})$ in moment space. The expressions for the strain-rate tensor are generalizations of those given in [65].

Acknowledgments

This work was supported by NASA under contract no. NNL06AA34P. The authors acknowledge access to the use of supercomputing resources at the National Center for Supercomputing Applications (NCSA) under grant no. CTS 060027.

References

[1] Krishnamurty, K., "Acoustic Radiation from Two-dimensional Rectangular Cutouts in Aerodynamic Surfaces," NACA TN-3487, 1955.

[2] Roshko, A., "Some Measurements of Flow in a Rectangular Cutout," NACA TN-3488, 1955.

[3] Maull, D. J., and East, L. F., "Three-Dimensional Flow in Cavities," *Journal of Fluid Mechanics*, Vol. 16, No. 4, Aug. 1963, pp. 620–632. doi:10.1017/S0022112063001014

[4] Rossiter, J. E., "Wind-Tunnel Experiments on the Flow over Rectangular Cavities at Subsonic and Transonic Speeds," Aeronautical Research Council, Reports and Memoranda No. 3438, London, 1964.

[5] Heller, H. H., Holmes, D. G., and Covert, E. E., "Flow-Induced Pressure Oscillations in Shallow Cavities," *Journal of Sound and Vibration*, Vol. 18, No. 4, 1971, pp. 545–553. doi:10.1016/0022-460X(71)90105-2

[6] Block, P. J. W., "Noise Response of Cavities of Varying Dimensions at

Subsonic Speeds," NASA TN D-8351, 1976.
[7] Sarohia, V., "Experimental Investigation of Oscillations in Flows over Shallow Cavities," *AIAA Journal*, Vol. 15, No. 7, 1977, pp. 984–991. doi:10.2514/3.60739
[8] Tracey, M. B., and Plentovich, E. B., "Characterization of Cavity Flow Fields Using Pressure Data Obtained at Subsonic and Transonic Speeds," NASA TM-4436, 1993.
[9] Ahuja, K. K., and Mendoza, J., "Effects of Cavity Dimensions, Boundary Layer, and Temperature on Cavity Noise with Emphasis on Data to Validate Computational Aeroacoustic Codes," NASA CR-4653, 1995.
[10] Forestier, N., Jacquin, L., and Geffroy, P., "The Mixing Layer over a Deep Cavity at High-Subsonic Speed," *Journal of Fluid Mechanics*, Vol. 475, Jan. 2003, pp. 101–145. doi:10.1017/S0022112002002537
[11] Faure, T., Adrianos, P., Lusseyran, F., and Pastur, L., "Visualization of the Flow inside an Open Cavity at Medium Range Reynolds Numbers," *Experiments in Fluids*, Vol. 42, No. 2, Feb. 2007, pp. 169–184. doi:10.1007/s00348-006-0188-8
[12] Gharib, M., and Roshko, A., "The Effect of Flow Oscillations on Cavity Drag," *Journal of Fluid Mechanics*, Vol. 177, Apr. 1987, pp. 501–530. doi:10.1017/S002211208700106X
[13] Bilanin, A. J., and Covert, E. E., "Estimation of Possible Excitation Frequencies for Shallow Rectangular Cavities," *AIAA Journal*, Vol. 11, No. 3, 1973, pp. 347–351. doi:10.2514/3.6747
[14] Tam, C. K., and Block, P. J. W., "On the Tones and Pressure Oscillations Induced by Flow over Rectangular Cavities," *Journal of Fluid Mechanics*, Vol. 89, No. 2, 1978, pp. 373–399. doi:10.1017/S0022112078002657
[15] Howe, M. S., *Acoustics of Fluid-Structure Interactions*, Cambridge Univ. Press, New York, 1998.
[16] Rockwell, D., and Naudascher, E., "Review-Self-Sustaining Oscillations of Flow Past Cavities," *Journal of Fluids Engineering*, Vol. 100, June 1978, pp. 152–165.
[17] Fuglsang, D., and Cain, A. B., "Evaluation of Shear Layer Cavity Resonance Mechanisms by Numerical Simulation," AIAA Paper 92-0555, 1992.
[18] Lamp, A. M., and Chokani, N., "Computation of Cavity Flows with Suppression Using Jet Blowing," *Journal of Aircraft*, Vol. 34, No. 4, 1997, pp. 545–551. doi:10.2514/2.2207
[19] Zhang, X., Rona, A., and Edwards, J. A., "The Effect of Trailing Edge Geometry on Cavity Flow Oscillation Driven by a Supersonic Shear Layer," *The Aeronautical Journal*, Vol. 102, No. 1013, Mar. 1998, pp. 129–136.
[20] Shieh, C. M., and Morris, P. J., "Parallel Numerical Simulation of Subsonic Cavity Noise," AIAA Paper 99-1891, 1999.
[21] Colonius, T., Basu, A. J., and Rowley, C. W., "Numerical Investigation of the Flow Past a Cavity," AIAA Paper 99-1912, 1999.
[22] Colonius, T., Basu, A. J., and Rowley, C. W., "Computation of Sound Generation and Flow/Acoustic Instabilities in the Flow Past an Open Cavity," Third ASME/JSME Joint Fluids Engineering Conference, American Society of Mechanical Engineers Paper FEDSM 99-7228, 1999.
[23] Rowley, C. W., Colonius, T., and Basu, A., "On Self-Sustained Oscillations in Two-Dimensional Compressible Flow over Rectangular Cavities," *Journal of Fluid Mechanics*, Vol. 455, Mar. 2002, pp. 315–346. doi:10.1017/S0022112001007534
[24] Brès, G. A., and Colonius, T., "Three-Dimensional Instabilities in Compressible Flow over Open Cavities," *Journal of Fluid Mechanics*, Vol. 599, Mar. 2008, pp. 309–339. doi:10.1017/S0022112007009925
[25] Smagorinsky, J., "General Circulation Experiments with Primitive Equations 1: The Basic Equations," *Monthly Weather Review*, Vol. 91, No. 3, Mar. 1963, pp. 99–164. doi:10.1175/1520-0493(1963)091<0099:GCEWTP>2.3.CO;2
[26] Dubief, Y., and Delcayre, F., "On Coherent Structure Identification in Turbulence," *Journal of Turbulence*, Vol. 1, No. 11, Dec. 2000, pp. 1–22. doi:10.1088/1468-5248/1/1/011
[27] Gloerfelt, X., Bogey, C., and Bailly, C., "LES of the Noise Radiated by a Flow over a Rectangular Cavity," *International Workshop on LES of Acoustics* [CD-ROM], DLR, Germany Aerospace Center, Gottingen, Germany, 2002.
[28] Larcheveque, L., Sagaut, P., Le, T., and Comte, P., "Large Eddy Simulation of a Compressible Flow in a Three-Dimensional Open Cavity at High Reynolds number," *Journal of Fluid Mechanics*, Vol. 516, Oct. 2004, pp. 265–301. doi:10.1017/S0022112004000709
[29] Larcheveque, L., Sagaut, P., and Labbe, O., "Large Eddy Simulation of a Subsonic Cavity Flow including Asymmetric Three-Dimensional Effects," *Journal of Fluid Mechanics*, Vol. 577, Apr. 2007, pp. 105–126. doi:10.1017/S0022112006004502
[30] Suponitsky, V., Avital, E., and Gaster, M., "On the Three-Dimensionality and Control of Incompressible Cavity Flow," *Physics of Fluids*, Vol. 17, Oct. 2005, Paper 104103.
[31] Shieh, C. M., and Morris, P. J., "Comparison of Two- and Three-Dimensional Turbulent Cavity Flows," AIAA Paper 2001-16385, 2007.
[32] Spalart, P. R., and Allmaras, S. R., "One-Equation Turbulence Model for Aerodynamic Flows," *La Recherche Aérospatiale*, Vol. 1, No. 1, 1994, pp. 5–21.
[33] Colonius, T., "An Overview of Simulation, Modeling, and Active Control of Flow/Acoustic Resonance in Open Cavities," AIAA Paper 2001-0076, 2001.
[34] Rowley, C. W., and Williams, D. R., "Dynamics and Control of High-Reynolds Number Flow over Cavities," *Annual Review of Fluid Mechanics*, Vol. 38, Jan. 2006, pp. 251–276. doi:10.1146/annurev.fluid.38.050304.092057
[35] Chen, S., and Doolen, G., "Lattice Boltzmann Method for Fluid Flows," *Annual Review of Fluid Mechanics*, Vol. 30, Jan. 1998, pp. 329–364. doi:10.1146/annurev.fluid.30.1.329
[36] Succi, S., *The Lattice Boltzmann Equation for Fluid Dynamics and Beyond*, Clarendon Press, Oxford, 2001.
[37] Yu, D., Mei, R., Luo, L.-S., and Shyy, W., "Viscous Flow Computations with the Method of Lattice Boltzmann Equation," *Progress in Aerospace Sciences*, Vol. 39, No. 5, July 2003, pp. 329–367. doi:10.1016/S0376-0421(03)00003-4
[38] Nourgaliev, R. R., Dinh, T. N., Theofanous, T. G., and Joseph, D., "The Lattice Boltzmann Equation Method: Theoretical Interpretation, Numerics and Implications," *International Journal of Multiphase Flow*, Vol. 29, No. 1, Jan. 2003, pp. 117–169. doi:10.1016/S0301-9322(02)00108-8
[39] Premnath, K. N., McCracken, M. E., and Abraham, J., "A Review of Lattice Boltzmann Methods for Multiphase Flows Relevant to Engine Sprays," *SAE Transactions: Journal of Engines*, Vol. 113, 2005, pp. 929–940.
[40] Chen, H., Kandasamy, S., Orszag, S., Shock, R., Succi, S., and Yakhot, V.,"Extended Boltzmann Kinetic Equation for Turbulent Flows," *Science*, Vol. 301, No. 5633, Aug. 2003, pp. 633–636. doi:10.1126/science.1085048
[41] Dong, Y., Sagaut, P., and Marie, S., "Inertial Range Consistent Subgrid Model for Large-Eddy Simulation Based on Lattice-Boltzmann Method," *Physics of Fluids*, Vol. 20, Mar. 2008, Paper 035105. doi:10.1063/1.2842381
[42] Shan, X., Yuan, X.-F., and Chen, H., "Kinetic Theory Representation of Hydrodynamics: A Way Beyond the Navier-Stokes Equation," *Journal of Fluid Mechanics*, Vol. 550, Mar. 2006, pp. 413–441. doi:10.1017/S0022112005008153
[43] Philippi, P. C., Hegele, L. A., and Santos, L., "From the Continuous to the Lattice Boltzmann Equation: The Discretization Problem and Thermal Models," *Physical Review E (Statistical Physics, Plasmas, Fluids, and Related Interdisciplinary Topics)*, Vol. 73, May 2006, Paper 056702. doi:10.1103/PhysRevE.73.056702
[44] Chikatamarla, S. S., Ansumali, S., and Karlin, I. V., "Entropic Lattice Boltzmann Models for Hydrodynamics in Three Dimensions," *Physical Review Letters*, Vol. 97, July 2006, Paper 010201. doi:10.1103/PhysRevLett.97.010201
[45] Buick, J. M., Greated, C. A., and Campbell, D. M., "Lattice BGK Simulation of Sound Waves," *Europhysics Letters*, Vol. 43, No. 3, Aug. 1998, pp. 235–240. doi:10.1209/epl/i1998-00346-7
[46] Buick, J. M., Buckley, C. L., Greated, C. A., and Gilbert, J., "Lattice Boltzmann BGK Simulation of Nonlinear Sound Waves: The Development of a Shock Front," *Journal of Physics A*, Vol. 33, No. 21, June 2000, pp. 3917–3928. doi:10.1088/0305-4470/33/21/305
[47] Mallick, S., Shock, R., and Yakhot, V., "Numerical Simulation of the Excitation of a Helmholtz Simulator by a Grazing Flow," *Journal of the Acoustical Society of America*, Vol. 114, No. 4, Oct. 2003, pp. 1833–1840. doi:10.1121/1.1606464
[48] Wilde, A., "Calculation of Sound Generation and Radiation from

Instationary Flows," *Computers and Fluids*, Vol. 35, Nos. 8–9, 2006, pp. 986–993.
doi:10.1016/j.compfluid.2005.03.005

[49] Li, X. M., So, R. M. C., and Leung, C. K., "Propagation Speed, Internal Energy, and Direct Aeroacoustics Simulations Using Lattice Boltzmann Method," *AIAA Journal*, Vol. 44, No. 12, 2006, pp. 2896–2903.
doi:10.2514/1.18933

[50] Kam, E.W.S., So, R. M. C., and Leung, R. C. K., "Lattice Boltzmann Method Simulation of Aeroacoustics and Nonreflecting Boundary Conditions," *AIAA Journal*, Vol. 45, No. 7, 2007, pp. 1703–1762.
doi:10.2514/1.27632

[51] Marië, S., Ricot, D., and Sagaut, P., "Accuracy of Lattice Boltzmann Method for Aeroacoustic Simulations," 13th AIAA/CEAS Aeroacoustics Conference, AIAA Paper 2007-3515, 2007.

[52] Lew, P.-T., Lyrintzis, A., Crouse, B., Balasubramanian, G., Freed, D., and Mongeau, L., "Noise Prediction of a Subsonic Turbulent Round Jet Using the Lattice–Boltzmann Method," 13th AIAA/CEAS Aeroacoustics Conference, AIAA Paper 2007-3636, 2007.

[53] Tsutahara, M., Kataoka, T., Shikata, K., and Takada, N., "New Model and Scheme for Compressible Fluids of the Finite Difference Lattice Boltzmann Method and Direct Simulations of Aerodynamic Sound," *Computers and Fluids*, Vol. 37, No. 1, Jan. 2008, pp. 79–89.
doi:10.1016/j.compfluid.2005.12.002

[54] Bhatnagar, P. L., Gross, E. P., and Krook, M., "A Model for Collision Processes in Gases 1: Small Amplitude Processes in Charged and Neutral One-Component Systems," *Physical Review E (Statistical Physics, Plasmas, Fluids, and Related Interdisciplinary Topics)*, Vol. 94, No. 3, 1954, pp. 511–525.

[55] Qian, Y., d'Humières, D., and Lallemand, P., "Lattice BGK models for Navier-Stokes Equations," *Europhysics Letters*, Vol. 17, No. 6, Feb. 1992, pp. 479–484.
doi:10.1209/0295-5075/17/6/001

[56] Chen, H., Chen, S., and Matthaeus, W. H., "Recovery of the Navier–Stokes Equations Using a Lattice–Gas Boltzmann Method," *Physical Review A*, Vol. 45, No. 8, 1992, pp. R5339–R5342.
doi:10.1103/PhysRevA.45.R5339

[57] d'Humières, D., *Generalized Lattice Boltzmann Equations*, edited by B. D. Shigal, and D. P. Weaver, Progress in Aeronautics and Astronautics, Vol. 450, AIAA, Washington, D.C., 1992, pp. 450–458.

[58] Lallemand, P., and Luo, L.-S., "Theory of the Lattice Boltzmann Method: Dispersion, Dissipation, Isotropy, Galilean Invariance, and Stability," *Physical Review E (Statistical Physics, Plasmas, Fluids, and Related Interdisciplinary Topics)*, Vol. 61, No. 6, 2000, pp. 6546–6562.
doi:10.1103/PhysRevE.61.6546

[59] d'Humières, D., Ginzburg, I., Krafczyk, M., Lallemand, P., and Luo, L.-S., "Multiple-Relaxation-Time Lattice Boltzmann Models in Three Dimensions," *Philosophical Transactions of the Royal Society of London, Series A: Mathematical and Physical Sciences*, Vol. 360, No. 1792, Mar. 2002, pp. 437–451.
doi:10.1098/rsta.2001.0955

[60] McCracken, M. E., and Abraham, J., "Multiple-Relaxation-Time Lattice–Boltzmann Model for Multiphase Flow," *Physical Review E (Statistical Physics, Plasmas, Fluids, and Related Interdisciplinary Topics)*, Vol. 71, Mar. 2005, Paper 036701.
doi:10.1103/PhysRevE.71.036701

[61] Premnath, K. N., and Abraham, J., "Three-Dimensional Multi-Relaxation Time (MRT) Lattice–Boltzmann Models for Multiphase Flow," *Journal of Computational Physics*, Vol. 224, No. 2, June 2007, pp. 539–559.
doi:10.1016/j.jcp.2006.10.023

[62] Premnath, K. N., and Abraham, J., "Simulations of Binary Drop Collisions with a Multiple-Relaxation-Time Lattice–Boltzmann Model," *Physics of Fluids*, Vol. 17, 2005, Paper 122105.
doi:10.1063/1.2148987

[63] Pattison, M. J., Premnath, K. N., Morley, N. B., and Abdou, M., "Progress in Lattice Boltzmann Methods for Magnetohydrodynamic Flows Relevant to Fusion Applications," *Fusion Engineering and Design*, Vol. 83, No. 4, May 2008, pp. 557–572.
doi:10.1016/j.fusengdes.2007.10.005

[64] Krafczyk, M., Tölke, J., and Luo, L.-S., "Large-Eddy Simulations with a Multiple-Relaxation-Time LBE Model," *International Journal of Modern Physics B*, Vol. 17, Nos. 1–2, Jan. 2003, pp. 33–39.
doi:10.1142/S0217979203017059

[65] Yu, H., Luo, L.-S., and Girimaji, S. S., "LES of Turbulent Square Jet Flow Using an MRT Lattice Boltzmann Model," *Computers and Fluids*, Vol. 35, Nos. 8–9, 2006, pp. 957–965.
doi:10.1016/j.compfluid.2005.04.009

[66] Premnath, K. N., Pattison, M. J., and Banerjee, S., "Generalized Lattice Boltzmann Equation with Forcing Term for Computation of Wall Bounded Turbulent Flows," *Physical Review E (Statistical Physics, Plasmas, Fluids, and Related Interdisciplinary Topics)* (submitted for publication).

[67] Guo, Z., Zheng, C., and Shi, B., "Discrete Lattice Effects on the Forcing Term in the Lattice Boltzmann Method," *Physical Review E (Statistical Physics, Plasmas, Fluids, and Related Interdisciplinary Topics)*, Vol. 65, No. 4, Apr. 2002, Paper 046308.
doi:10.1103/PhysRevE.65.046308

[68] He, X., Shan, X., and Doolen, G. D., "A Discrete Boltzmann Equation Model for Non-Ideal Gases," *Physical Review E (Statistical Physics, Plasmas, Fluids, and Related Interdisciplinary Topics)*, Vol. 57, No. 1, 1998, pp. R13–R16.
doi:10.1103/PhysRevE.57.R13

[69] van Driest, E. R., "On the Turbulent Flow Near a Wall," *Journal of the Aeronautical Sciences*, Vol. 23, No. 11, 1956, pp. 1007–1011.

[70] Pope, S., *Turbulent Flows*, Cambridge Univ. Press, New York, 2000.

[71] Sagaut, P., *Large-Eddy Simulation for Incompressible Flows—An Introduction*, 2nd edition, Springer–Verlag, New York, 2002.

[72] Moin, P., and Kim, J., "Numerical Investigation of Turbulent Channel Flow," *Journal of Fluid Mechanics*, Vol. 118, May 1982, pp. 341–377.
doi:10.1017/S0022112082001116

[73] Bouzidi, M., Firdaouss, M., and Lallemand, P., "Momentum Transfer of a Boltzmann–Lattice Fluid with Boundaries," *Physics of Fluids*, Vol. 13, Nov. 2001, pp. 3452–3459.

[74] Ladd, A. J. C., "Numerical Simulations of Particulate Suspensions via a Discretized Boltzmann Equation," *Journal of Fluid Mechanics*, Vol. 271, July 1994, pp. 285–309.
doi:10.1017/S0022112094001771

[75] Chen, S., Martinez, D., and Mei, R., "On Boundary Conditions in Lattice Boltzmann Method," *Physics of Fluids*, Vol. 8, Sept. 1996, pp. 2527–2536.

[76] Powell, A., "On the Edgetone," *Journal of the Acoustical Society of America*, Vol. 33, No. 4, Apr. 1961, pp. 395–409.
doi:10.1121/1.1908677

[77] Banerjee, S., Premnath, K. N., and Pattison, M. J., "Turbulence Simulation Using the Generalized Lattice Boltzmann Equation on Massively Parallel Architectures," *Third Asian-Pacific Congress on Computational Mechanics in Conjunction with Eleventh International Conference on Enhancement and Promotion of Computational Methods in Engineering and Science (APCOM '07–EPMESC XI)* [CD-ROM], Asian-Pacific Association for Computational Mechanics, Kyoto, Japan, 2007.

[78] Pattison, M. J., Premnath, K. N., and Banerjee, S., "Turbulence-Induced Secondary Flows in a Square Duct Using a Multiple-Relaxation Time Lattice-Boltzmann Approach," *Turbulence and Shear Flow Phenomena (TSFP-5)* [CD-ROM], Technische Univ. München, Munich, 2007.

[79] Henderson, B., "Automobile Noise Involving Feedback-Sound Generation by Low Speed Cavity Flows," *Third Computational Aeroacoustics Workshop on Benchmark Problems*, CP-2000-209790, NASA, 2000, pp. 363–370.

[80] Kurbatskii, K., and Tam, C. K., "Direct Numerical Simulation of Automobile Cavity Tones," NASA CP-2000-209790, 2000, pp. 371–383.

[81] Shieh, C. M., and Morris, P. J., "Parallel Numerical Simulation of Automobile Noise Involving Feedback," NASA CP-2000-209790, 2000, pp. 363–370.

[82] Moon, Y. J., Koh, S. R., Cho, Y., and Chung, J. M., "Aeroacoustic Computations of the Unsteady Flows over a Rectangular Cavity with a Lip," NASA CP-2000-209790, 2000, pp. 347–353.

[83] Hardin, J. C., and Pope, D. S., "An Acoustic/Viscous Splitting Technique for Computational Aeroacoustics," *Theoretical and Computational Fluid Dynamics*, Vol. 6, Nos. 5–6, 1994, pp. 323–340.
doi:10.1007/BF00311844

[84] Gaster, M., "Growth of Disturbances in Both Space and Time," *Physics of Fluids*, Vol. 11, Apr. 1968, pp. 723–727.

[85] Huerre, P., and Monkewitz, P. A., "Absolute and Convective Instabilities in Free Shear Layers," *Journal of Fluid Mechanics*, Vol. 159, Oct. 1985, pp. 151–168.
doi:10.1017/S0022112085003147

[86] Tam, C. K., "The Acoustic Modes of a Two-Dimensional Rectangular Cavity," *Journal of Sound and Vibration*, Vol. 49, No. 3, Oct. 1976, pp. 353–364.
doi:10.1016/0022-460X(76)90426-0

P. Givi
Associate Editor